

# Applying Droplets and Films in Evaporative Lithography

K.S. Kolegov<sup>a,b,c</sup>, L. Yu. Barash<sup>c,\*</sup>

<sup>a</sup>Astrakhan State University, 414056 Astrakhan, Russia

<sup>b</sup>Volga State University of Water Transport, Caspian Institute of Maritime and River Transport, 414014 Astrakhan, Russia

<sup>c</sup>Landau Institute for Theoretical Physics, 142432 Chernogolovka, Russia

## Abstract

This review covers experimental results of evaporative lithography and analyzes existing mathematical models of this method. Evaporating droplets and films are used in different fields, such as cooling of heated surfaces of electronic devices, diagnostics in health care, creation of transparent conductive coatings on flexible substrates, and surface patterning. A method called evaporative lithography emerged after the connection between the coffee ring effect taking place in drying colloidal droplets and naturally occurring inhomogeneous vapor flux densities from liquid–vapor interfaces was established. Essential control of the colloidal particle deposit patterns is achieved in this method by producing ambient conditions that induce a nonuniform evaporation profile from the colloidal liquid surface. Evaporative lithography is part of a wider field known as “evaporative-induced self-assembly” (EISA). EISA involves methods based on contact line processes, methods employing particle interaction effects, and evaporative lithography. As a rule, evaporative lithography is a flexible and single-stage process with such advantages as simplicity, low price, and the possibility of application to almost any substrate without pretreatment. Since there is no mechanical impact on the template in evaporative lithography, the template integrity is preserved in the process. The method is also useful for creating materials with localized functions, such as slipperiness and self-healing. For these reasons, evaporative lithography attracts increasing attention and has a number of noticeable achievements at present. We also analyze limitations of the approach and ways of its further development.

**Keywords:** Evaporative lithography, drops, liquid films, colloidal liquids, micro- and nanostructures, functional coatings.

## 1. Introduction

The drying of droplets and films on solid surfaces is accompanied by a number of phenomena of general physical interest. As a result of evaporation, the deposition patterns of particles contained in the liquid can be spatially structured in one or another way depending on the experimental conditions. This process has proved to be technologically involved in many applied studies and has led to the development of the evaporative lithography method addressed in this review.

Before proceeding to the main subject of the review, we briefly describe the basic physical processes that occur in evaporating droplets and films. These open systems exchange mass and energy with the environment, and their complex behavior is due to many factors. Various physical and chemical properties of the liquid solution, substrate, and ambient air as well as external forces affect the evaporation mode.

Of the many physical processes occurring in droplet and film systems, the basic process is droplet evaporation into the surrounding gas, which since Maxwell’s studies has long been regarded as mainly vapor diffusion from the droplet surface (also see [1, 2, 3]). The classic quasistationary theory of droplet evaporation does not include the effects of fluid dynamics in the

droplet and only partially takes the simplest elements of heat transfer into account.

In the last twenty years, the evaporation of droplets and films has attracted renewed attention due to the development of new applications such as the evaporation and combustion of fuel droplets in engines [4, 5], the interaction of droplets with surfaces of varying wettability in jet printing [6], the deposition of microarrays of DNA and RNA molecules [7, 8], pattern formation on surfaces [9, 10], disease diagnostics techniques [11], the creation of photonic crystals [12, 13, 14], the production of nanoparticles [15], the production of stable ultrathin film coatings of polar liquids [16], cooling of devices [17, 18, 19], removal of nanoparticles from a solid surface for cleaning purposes [20], etc.

The problem of the evaporation of droplets and films containing nanoparticles aroused a large interest. Nanoparticle structures can appear on the free surface during evaporation and also remain on the substrate after drying. One of the examples is the self-assembly of nanoparticles into organized superlattices (see, e.g., [21]).

The presence of substrate nonuniformity and defects normally causes effective fixation (pinning) of the three-phase boundaries of sessile droplets. Observation of different evaporation process stages [22, 23, 24, 25] has shown that the longest and dominant regime of the evaporation process is where the contact line is pinned and the contact area of a drop with a solid

\*Corresponding author.

Email address: barash@itp.ac.ru (L. Yu. Barash)

base remains constant. As the volume of the sessile droplet decreases, periodic displacements and fixations of the contact line can occur. As the contact line further becomes completely depinned, a different regime, the constant contact angle mode, switches on. In the final drying stage, the height, the contact area, and the contact angle rapidly decrease with time.

Among the processes of spatial structuring of deposition patterns from drying sessile droplets, the best known is the so-called coffee-ring effect, which is observed in evaporating droplets of colloidal and molecular solutions if the deposits are formed near the pinned contact line. The studies of Deegan et al. theoretically proved that mass loss resulting from vaporization occurs nonuniformly along the free surface of the liquid layer, significantly increasing near the contact line [26, 27, 28]. Because the evaporation rate dominates at the droplet periphery, compensatory flows are generated that transfer suspended and dissolved matter to the three-phase boundary, resulting in an annular distribution of deposited particles near the contact line. The number of concentric structures of particles formed on the substrate depends on the number of periodic modes of displacement and fixation of the contact line, which can occur with a decrease in the droplet volume [28]. The behavior of the three-phase boundary and the type of annular deposition, including the presence of cracks, depend on the substrate roughness and particle size [29].

A nonuniform mass flow during evaporation and the corresponding heat transfer result in more than just a compensatory flow. They also change the temperature distribution along the droplet surface, and because the surface tension depends on temperature, this can cause Marangoni forces. These forces produce thermocapillary convection inside a droplet [30, 31], which differs qualitatively from classical Marangoni convection studied in systems with a simple flat geometry [32, 33]. Under certain conditions, the value of the thermal conductivity of the substrate determines the tangential component of the temperature gradient at the droplet surface near the contact line and consequently affects the direction of convection inside the droplet [34, 35].

In the presence of thermocapillary flows, some of the colloidal particles are sometimes deposited in the central part of the droplet, thus forming a spot inside the ring [36]. A uniform distribution of the deposit over the entire area where the liquid had previously come into contact with the substrate can be due to the effect of the capture of colloidal particles by the descending free surface [37]. A similar pattern is obtained when a surfactant and a surface-absorbed polymer are added to a binary mixture [38]. When salt is added, its crystallization is observed in the deposit in some cases [39, 40, 41]. More details about methods for suppressing the coffee-ring effect to obtain uniform deposits can be found in [42].

For rather large contact angles  $\theta$ , the thermocapillary flow can significantly exceed the compensatory flow. But with small  $\theta$ , the compensatory flow dominates the Marangoni convection for the following reasons. First, the Marangoni flow velocity is proportional to  $\theta^2$  and decreases rapidly in the final stage of the evaporation process. Second, the thermocapillary instability is known to occur only when the Marangoni number

$Ma = -\sigma' \Delta T h_0 / (\eta \kappa)$  exceeds a certain critical value. Here,  $\Delta T$  is the temperature difference between the apex and the substrate,  $\sigma'$  is the temperature-based derivative of the surface tension,  $h_0$  is the droplet height,  $\eta$  is the fluid viscosity, and  $\kappa$  is the thermal diffusivity. The threshold value for a flat fluid film is about 80 [33]. The onset of Marangoni convection was also confirmed in [43] in the particular case of droplets with the contact angle  $\theta = 90^\circ$ .

There are other hydrodynamic effects in droplets and films, which in some cases play a role in obtaining structured deposits. Solutal Marangoni flow is due to the influence of surfactants on the surface tension of the solution. For example, it was shown in [44] that this flow can generate ring-shaped stains in the case of a drop of salt solution. Finger-like instability in films and droplets can occur when surfactants are present [45]. The thermocapillary rupture in a film flowing down a tilted plate was observed in the local heating point [46]. The Leidenfrost effect is another example of a classic effect in droplet–film systems that is actively used and studied and can affect a pattern formation [47, 48, 49, 50].

The heterogeneous heat and mass transfer in an evaporating liquid is an essential condition for the emergence of structured deposits not only in the case of the coffee-ring effect but also in many other problem statements. In liquid sessile droplets, such processes naturally occur in the vicinity of the contact line. Heterogeneities in droplets and liquid films can also be induced by producing ambient conditions described below. The ability to create structures in a controlled manner using such external influences is the fundamental in the evaporative lithography method.

Progress in understanding the coffee-ring effect and other physical processes occurring in evaporating droplets and films, substantial developments in experimental research, and the wide interest in these phenomena in many applications led to the significant activity of experimenters and theorists in this field over the last twenty years. Review papers cover many details of this subject: dynamics and evolution of thin liquid films [51], spreading of surfactants in thin liquid films [52], structural evolution of drying droplets of biological liquids [53, 54], condensation and coalescence of droplets [55], wetting and spreading effects [56, 57, 58], organized structures of particles on a substrate [59, 60, 61], inkjet-printed photonic crystal structures [13], evaporation of thin films of colloidal solutions [62], self-assembly of 3D structures of nano- and microparticles [63], hydrothermal waves in evaporating sessile droplets and the effect of substrate properties [64], mass transport in evaporating droplets [65, 66], stain geometry during evaporation of a surfactant solution [67], evaporation of nanoparticle-laden droplets [68], control of Marangoni convection in liquid films [69], hydrodynamics in thin liquid films [70], properties and applications of liquid marbles (droplets wrapped by micro- and nanoparticles) [71], heat and mass transfer near the liquid–gas interface on heated substrates [72], methods for self-assembly of monolayers of colloidal particles [73], mitigation, suppression, and use of the coffee-ring effect [42, 74], wetting and evaporation effects [75], deposits appearing on a substrate after drying of multicomponent droplets [76], hy-

dromechanical and mechanical instabilities during drying of solution droplets [77], heat transfer associated with the liquid-vapor phase change on functional micro- and nanostructured surfaces [78], stratification of particles upon drying of colloidal films [79], multiscale assembly of organic electronics [80], simulation of spreading of surfactant-laden droplets [81], and the role of surfactants in obtaining structures on substrates [82]. The self-assembly of organized structures during evaporation was reviewed in monographs [83, 84], evaporation and wetting, in books [85, 86], and cracks occurring during drying and associated structures, in [87].

Many methods for obtaining structured deposits based on the self-assembly of micro- and nanoparticles as a result of evaporation have been proposed [88]. The studies in this direction are known as “evaporative-induced self-assembly” (EISA). For example, EISA is actively used to produce porous mesostructures [89, 90, 91, 92]. Here, we propose the following classification of EISA methods (Fig. 1). Of course, this division into subgroups is very tentative, and some approaches can often simultaneously combine principles that are characteristic of different subgroups. The first subgroup of methods is based on using contact line processes (“contact line methods” in Fig. 1). For example, a plate is placed above the film. It can be flat [93, 94]. Sometimes, the plate is characterized by a varying curvature due to swelling [95]. In other cases, its geometry is a spherical segment [96, 97], a semicylinder form [98], an ad hoc geometric shape [99], or a template with groove/ridge surface topography [100]. Normally, the substrate is immobile throughout the process. For example, in the experiment [101], the substrate was heated to 130–140 °C to obtain a conductive and transparent structured thin film of nanotubes used in flexible electronics. The creation of periodic nanotube stripes can be controlled with surfactants [102]. In another experiment [103], the substrate was slowly displaced relative to the plate located at a slight angle. This allowed obtaining a prolonged film of perovskite. Such photoactive layers can be used as flat solar cells. A periodic deposition pattern of a binary colloid mixture can be also obtained under a moving plate [104]. This method was improved in [105] by using an oscillating blade and a bending actuator. This provides an additional possibility to manage the pattern being formed. One more key parameter of this technique is the oscillation frequency of the blade tip. The mentioned EISA methods are normally based on the capillary bridge and stick-slip motion effect [96] (see Fig. 1). Essentially, it includes wetting two surfaces by a film in the gap between them [96] and mass transfer with a capillary flow toward the contact line where intensive evaporation occurs. Sometimes, the contact line moves periodically, which generates concentric deposits [8, 106, 107]. This also applies to the drying of a liquid film with nanoparticles on the surface of a layer of another liquid [108]. Sometimes, fingering instabilities produce spoke patterns [97]. The authors of [98] experimented with DNA nanowires and concluded that spoke patterns can be obtained instead of concentric rings by changing the pH of the solution. The drying deposition method on a vertical plate works by the same principle [109, 110, 111] (see Fig. 1). A meniscus is formed near the plate as a result of liquid wetting.

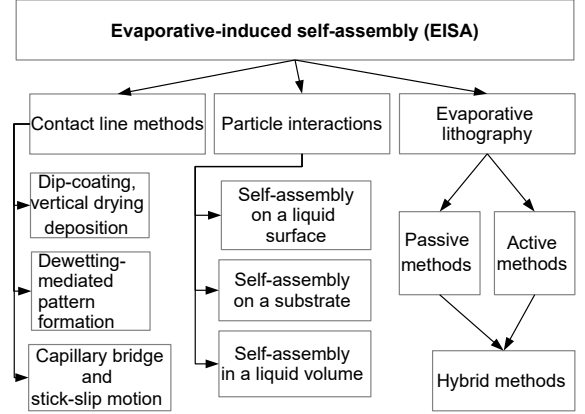


Figure 1: EISA methods classification.

The capillary flow transfers particles into this area. As the fluid dries, a particle layer or a periodic pattern is thus formed on the plate. If the plate is withdrawn with some velocity, this is the dip-coating method [112, 113, 114]. For example, the authors of [115] used dip-coating to produce organic transistors. We also mention the Langmuir–Blodgett method, which is close to dip-coating. This technique transfers a layer of particles from the liquid surface to a solid surface [116, 117]. The formation of micro- and nanoparticle structures often occurs in areas of film rupture and as the dry patch expands further [118, 119, 120]. This method is known as dewetting-mediated pattern formation, which is also included in the subgroup of contact line methods (Fig. 1). In review [121], both passive and active experimental setups for controlling the contact line motion were described. Studying the three-phase boundary dynamics in such methods is essential because it has a significant impact on the sediment structure. We note that substantial progress has been achieved in studying the evaporation flux structure in the contact line area [122, 123, 124] and its effect on the formation of the wetting angle for evaporating sessile droplets with good wettability [125, 126, 127].

Another subgroup of methods is based on particle interaction forces (Fig. 1). These include electrostatic and intermolecular interaction forces (van der Waals forces) [128, 129, 130, 131]. We also mention the capillary particle interaction [132, 133, 134]. Particles assemble directly on the substrate [135, 136, 109], on the free liquid surface [21, 134, 137], or in the bulk [138, 139, 140].

Some methods are difficult to assign to EISA, but they also allow forming certain patterns. Silver nanowires were used in [141] to form stretchable electrodes with excellent electromechanical stability subjected to periodic mechanical deformation. An array of micron-sized droplets was applied by spray coating to the surface. The nanowires inside the microdroplets were bent into curved shapes by the elasto-capillary interaction while the microdroplets were moving toward the solid surface. After the droplets impacted on the substrate, rings were formed from overlapping elastic nanowires. Such structures can well tolerate bending and stretching while retaining their electrical conductive properties [141].

The above methods of forming structured coatings are difficult to control, especially in real-time. The precise pattern except its qualitative properties is hard to predict. Although work is also progressing in this direction [103, 105, 100], another logical continuation of the development of these methods is the emergence of a narrower direction called “evaporative lithography” (Fig. 1). According to the theory of Deegan et al., which explained the coffee-ring effect, it is possible to control the particle sedimentation process by manipulating the vapor concentration near the two-phase boundary [26, 27, 28]. The method called “evaporative lithography” [142, 143] was developed based on this theory. The essence of this method is to create ambient conditions for nonuniform evaporation from the colloidal liquid surface.

There are other lithographic approaches to creating polymer coatings with topographic patterns at the micro- and nanoscales. Structured colloidal assemblies are sometimes created on electrically [144, 145] and topographically modified substrate surfaces [146, 147, 148, 149]. But such approaches are not easy to apply to other classes of soft materials. In nanoimprint lithography, the template is in contact with the surface under pressure [150]. This sometimes leads to defects in the template itself. Such defects affect the shape of the resulting patterns. Evaporative lithography implies no mechanical impact on a template. Therefore, its integrity is preserved in the process. The method of photolithography is widely known, but this multistage process requires special equipment and materials [151]. Structured surfaces of polymers can be obtained by different molding methods, such as nanoscale injection molding [152], capillary molding [153], and ultraviolet nanoimprinting [154]. These methods have a number of disadvantages, such as lack of process flexibility and the need for expensive equipment. Nanosphere lithography (colloidal bead self-assembly) allows obtaining regular structures only of a single spatial shape when nanoparticles are deposited in the cavities between densely packed microspheres [155, 156, 157, 158]. Microstereolithography requires using special materials (photopolymers) [159, 160]. Moreover, there is often a problem of the destruction of the printed 3D microstructure under the influence of capillary forces (the stiction problem) [159, 160].

The EISA methods and, in particular, evaporative lithography are usually one-step methods. They do not require expensive equipment and materials. Moreover, they can be applied to almost any surfaces. Evaporative lithography, compared with other EISA methods, is a more flexible approach that allows considerable variation in the resulting patterns. In some cases, patterns are more stable (e.g., when particles are thermally or chemically sintered). Such methods are suitable for various applications in optical and microelectronics, health care, nanotechnologies, and other fields (see Sec. 2.4). Evaporative lithography therefore attracts increasing attention. Convection is caused by the nonuniform evaporation of colloidal film and transfers particles to the intense evaporation area. The vapor flow density can be controlled along the free surface of the liquid layer, for example, by placing a mask above the droplet [143]. The obtained structures replicate the shape of the mask holes, which play the role of templates. A template can be

not only a solid obstacle but also many other things (see Secs. 2 and 3 below). The method of evaporative lithography has two restrictions. First, the total evaporation time increases significantly because the mask blocks most of the liquid surface. Second, because glassy polymer particles are incapable of forming a solid film, only brittle coatings with cracks are obtained for polymer melting temperatures above room temperature without additional efforts. This problem is solved by introducing an IR source to the system [161]. Local heating creates intensive evaporation under holes in the mask. The particles heated by infrared light sinter well, and there are hence no cracks in the resulting structure. This method is simpler and cheaper and can be applied to almost any substrate without pretreatment compared with other methods of creating textured layers. For example, evaporative lithography was used experimentally [162] to demonstrate the possibility of creating materials with localized functions such as slipperiness and self-healing.

The purpose of this review is to present the existing achievements in evaporative lithography and to analyze how this method can be further developed. Section 2 deals with the main experimental works in this field. It describes passive, active, and hybrid methods of controlling the formation of colloidal particle structures (Fig. 1). It also provides examples of the practical use of these methods and discusses dimensionless parameters. Mathematical models of this class of phenomena are discussed in Sec. 3. The summary (Sec. 4) provides conclusions and discusses possible perspectives for the development of evaporative lithography.

## 2. Experimental achievements in evaporative lithography

### 2.1. Passive methods for controlling particle sedimentation

Existing evaporative lithography methods can be provisionally divided into passive and active methods. The difference is that active methods allow for real-time control of the pattern structure being formed, while passive methods do not provide such a possibility. The control in passive methods is achieved by adjusting key static parameters before starting the process. Examples of such parameters include the distance between the mask and liquid [143], the initial solution concentration [163], the size of mask holes [143], the substrate material [164] or tilt angle [165], the distance between two adjacent droplets [166, 167, 168, 169], the substrate temperature gradient (in case of nonuniform heating) [170], etc. In this section, we focus on describing experiments related to passive methods in evaporative lithography.

The experiment of Deegan et al. [27] showed a ring-shaped pattern (Fig. 2) formed as a result of intensive evaporation near the liquid–substrate–air boundary. The position of this ring corresponds to the location of the three-phase boundary (the pinned contact line). An analytic equation was derived in [28] to describe the ring width  $w(t)$  as a function of time,

$$w = R \sqrt{\frac{\phi}{4p}} \left[ 1 - \left( 1 - \frac{t}{t_{\max}} \right)^{\frac{3}{4}} \right]^{\frac{2}{3}},$$



where  $\phi$  is the volume fraction of colloidal particles,  $p$  is the packing density factor, and  $t$  and  $t_{\max}$  are the respective time and full time of evaporation. Under ambient conditions, the vapor flux density  $J(r, t)$  normally increases from the center ( $r = 0$ ) to the droplet periphery ( $r = R$ ), whose height is much less than the base radius ( $h(r = 0, t) \ll R$ ) [26]. The droplet base refers to the boundary where the liquid contacts the substrate. If the vapor flux density is uniform along the free surface of the droplet, a ring pattern is also formed (Fig. 2). Such a spatial function  $J$  can be obtained if the ambient humidity near the free droplet surface is relatively high. For this, the authors of [27] placed a substrate with a droplet on the water surface in a small container. In these two experiments, compensatory flows appeared that transferred the suspended matter to the contact line.

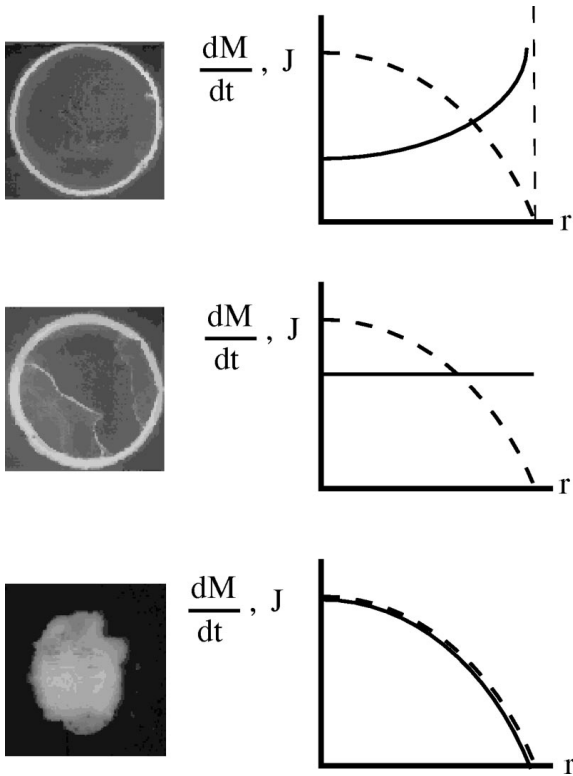


Figure 2: Types of deposits (left) and the corresponding types of the function  $J$  (solid line) relative to the droplet profile  $h$  (dashed line). Reproduced with permission from Ref. [27] (Copyright 2000 by The American Physical Society).

In the third experiment [27], the droplet was covered with a cap with a hole in the middle. As a result of intensive evaporation near the hole, compensatory flow carried the colloids to the central area. After the droplet dried, a spot-shaped deposit was observed on the substrate (Fig. 2). Based on the theoretical and experimental results, the authors of [27] formulated the idea of possible control of the deposition process by manipulating the vapor concentration around the droplet.

Another experimental team [142] performed measurements with a latex film drying on a substrate. The initial thickness of the liquid layer was 0.15 mm. In some places, evaporation was blocked by placing a coating with regularly spaced holes. The distance between the centers of adjacent holes was

16 mm. Such a coating was located in close proximity to the free surface of the film without the coating and film touching directly, but the gap between them was sufficiently small. This allowed evaporation to be blocked in certain local areas of the film. Figure 3 shows the structure of the latex film dried using this method [142].

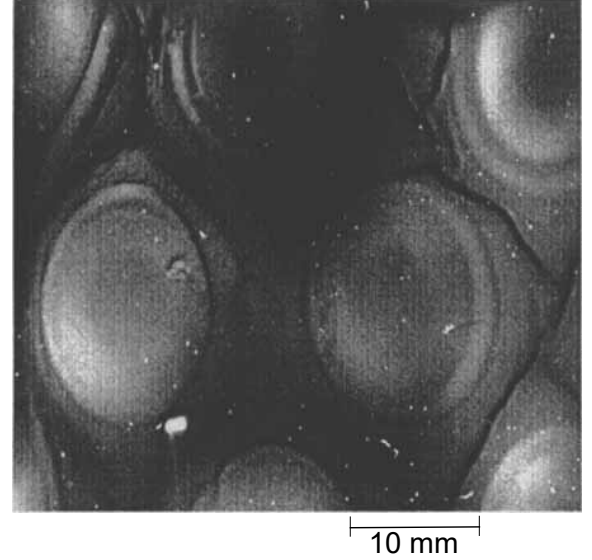


Figure 3: Film with selective evaporation in circular regions. Reprinted with permission from Ref. [142] (Copyright 1998, American Institute of Chemical Engineers (AIChE)).

The results of profilometry [142] showed that the maximum thickness of the final film is about 90  $\mu\text{m}$  in areas where evaporation occurred and about three times less in places where evaporation was suppressed.

The evaporation rate can be adjusted by selecting the liquid. For example, in [171], ethylene glycol is used, which evaporates relatively slowly. As a result, the capillary flow rate is less than 1  $\mu\text{m/s}$ . The flow slowly transfers microspheres to the wall of an open cylindrical cell. Nanoliter cells represent interest for labs-on-a-chip [171].

The term “evaporative lithography” was suggested in [143]. A mask with holes placed above the film surface was used in the experiment. The authors of [143] considered key parameters such as the initial volume fraction of the solution  $\phi_\mu$ , the mask design (geometric parameters), and the gap size between the film and the mask  $h_g$ . Masks contained a hexagonal array of holes of different diameters  $d_h$  with a pitch of  $P$  (distance between centers of adjacent holes). The resulting pattern consisted of individual particle aggregates several microns high. Their cross-sectional size was approximately equal to the value of  $d_h$ . Unary and binary colloidal films were investigated in [143]. Silica microspheres and polystyrene nanoparticles were taken. The authors of [143] estimated the microsphere sedimentation time by dividing the initial height of the film  $h_i$  by the Stokes velocity  $U_0 = 2a^2\Delta\rho g/(9\mu)$ , where  $a$  is the particle radius,  $\Delta\rho$  is the particle and water density difference,  $g$  is the acceleration of gravity, and  $\mu$  is the dynamic viscosity of the liquid. The full evaporation time ( $\approx 120$  min) significantly

exceeds the sedimentation time ( $\approx 2$  min). But in the case of a dilute solution, almost all particles migrated to the areas under holes. In our opinion, this is possible with weak adhesion of particles to the substrate that does not prevent their drift in the convection direction.

The influence of the initial volume fraction of the solution was studied at fixed values of the parameters  $d_h$ ,  $P$ , and  $h_g$  [143]. The value of  $\phi_\mu$  varied in the range from 0.005 to 0.3. Figure 4 shows optical images of the resulting deposits. Their patterns differ for different values of  $\phi_\mu$ . Discrete elements of sedimentation are formed under the holes when the initial volume fraction of particles is small (Fig. 4a). Their diameter  $d_f$  is relatively small,  $d_f < P$ . For  $\phi_\mu > \phi_\mu^*$ , the diameter of such elements  $d_f$  corresponds to the distance  $P$ ,  $d_f = P$ . In such cases, a relatively thick continuous film with a grooved surface is formed (Figs. 4b and 4c). Dome-shaped prominences can be seen under the holes (Fig. 4d). The critical initial volume fraction  $\phi_\mu^*$  of microparticles was defined in [143] based on geometric considerations,  $\phi_\mu^* \approx \pi\phi_f P / 200 \sqrt{3} h_i \approx 0.07$ , and experimentally (Fig. 4e). The volume fraction of randomly packed microspheres is  $\phi_f \approx 0.64$ .

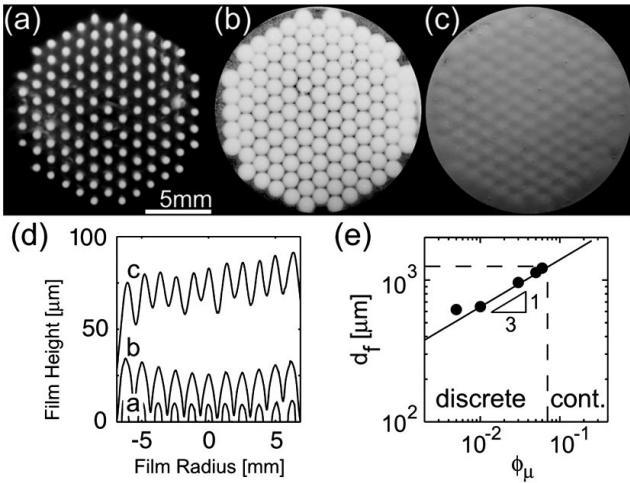


Figure 4: Optical images of the films obtained from colloidal suspensions with  $\phi_\mu =$  (a) 0.005, (b) 0.1, (c) 0.3; (d) the corresponding height profiles; (e) the dependence of the element diameter  $d_f$  on the initial volume fraction  $\phi_\mu$  of the solution. Reproduced with permission from Ref. [143] (Copyright 2007 by The American Physical Society).

The dependence of the dried film height difference  $\Delta h = h_{\max} - h_{\min}$  on the parameter  $h_g/P$  was measured at a fixed  $\phi_\mu$  for different  $d_h$ ,  $P$ , and  $h_g$  [143]. The value of  $\Delta h$  is small for  $h_g/P \geq 0.3$ , which evidences of the poor segregation of particles. As  $P$  increases with a fixed value of  $h_g/P$ , the value of  $\Delta h$  increases.

The process is somewhat different in the case of a two-component solution with volume fractions  $\phi_\mu = 0.3$  of microspheres and  $\phi_n = 10^{-3}$  of nanoparticles [143]. First, a continuous relief film is obtained from the microspheres. Second, nanoparticles assemble into discrete clusters under the holes in the mask. The porous medium formed by the presence of cavities between microspheres provides an additional driving force

to the nanoparticles. The pore radius is  $a_p \approx 0.15a_\mu$ , where  $a_\mu$  is the microsphere radius. Liquid residues in pores under the open area form menisci with capillary pressure induced at their surfaces. The pressure difference accelerates the transfer of nanoparticles to the places below the holes. Nanoparticles migrate into a network of cavities when the radius of the nanoparticles is  $a_{\text{nano}} \ll a_p$ . The dependence of the resulting particle distribution structure on the size ratio of micro- and nanoparticles in a binary system was studied separately in [172]. The plot (Fig. 5) shows that for  $a_\mu/a_{\text{nano}} \geq 7$ , the element diameter is close to the hole size ( $d_h = 250 \mu\text{m}$ ). The value 7 corresponds to the case where the size of nanoparticles is equal to the pore size.

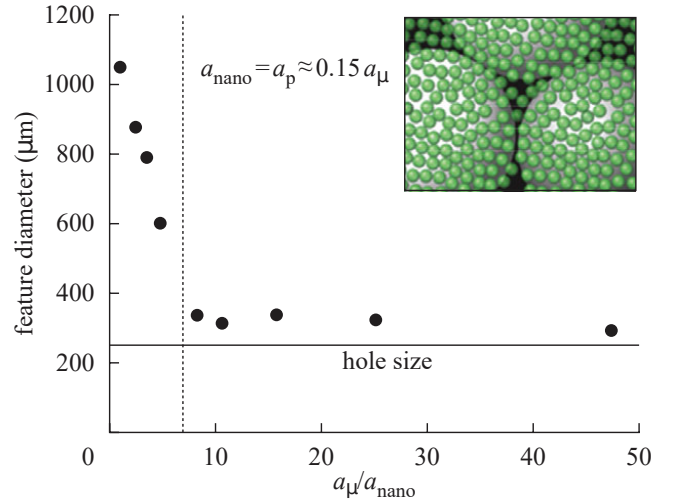


Figure 5: The diameter of the element (sedimentation of nanoparticles under the mask hole) as a function of  $a_\mu/a_{\text{nano}}$  (the inset schematically shows filling of pores between microspheres with nanoparticles for a high ratio of sizes). Reproduced from Ref. [172] with permission of the Royal Society.

The possibility of obtaining an inverted pattern from deposited particles was demonstrated in [163]. Under certain conditions, particles accumulate under covered areas of the mask. A sort of inverted pattern is thus obtained relative to the pattern of holes in the mask. Silica microspheres with a radius of  $492 \pm 58$  nm suspended in ethanol were used in [163]. The particles were stabilized in solution using a surfactant. The initial volume fraction  $\phi_i$  of the solution was varied in the range from 0.001 to 0.15. Fluorescence microscopy and tracers (a small fraction of particles was marked with fluorescent) were used in the experiment for direct observation and visualization of flows (see the Supplemental Material video [163]). Two types of masks were used: hexagonal arrays of circular holes and parallel strips. When the initial concentration of the solution is low, particles accumulate in the masked areas (Fig. 6a), where evaporation is slow. At the same time, a depleted zone appears under the holes and grows linearly with time (Fig. 6b). The fact is that with intense evaporation under the mask holes, the local temperature of the film surface decreases. The variation of temperature and the associated surface tension gradient lead to the Marangoni convection. This convection flow is directed from a low surface tension area to a high surface tension

area where the film surface temperature is relatively low. The typical particle velocity in such a flow is about  $10^{-3}$  m/s. For comparison, the velocity of the compensatory flow caused by evaporation is  $LE/h_i \approx 5 \times 10^{-7}$  m/s. Here,  $L = 2.5 \times 10^{-4}$  m is the typical size of the convection flow cell, the evaporation rate is  $E = 2.2 \times 10^{-7}$  m/s, and the initial film height is  $h_i = 10^{-4}$  m. Disappearance of the Marangoni effect was observed [163] when the solution reached a critical volume fraction  $\phi_c \approx 0.22$ . When the values of  $\phi_i$  are relatively high, structure inversion is not observed, because the system is mostly affected by the compensatory flow.

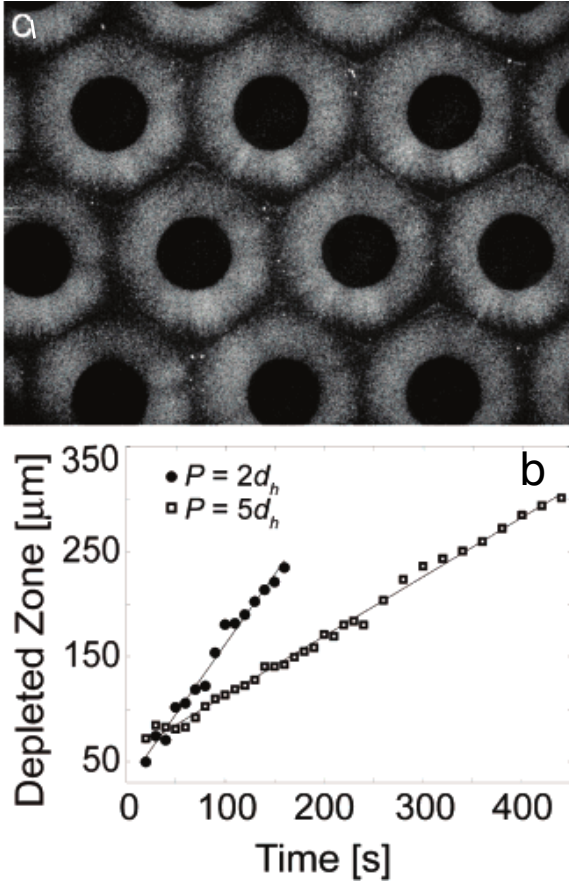


Figure 6: (a) Fluorescent image of the drying film ( $\phi_i=0.001$ ) at 190 s after placing the mask ( $d_h = 250$   $\mu$ m,  $P = 2d_h$ ); (b) an increase in the size of the depleted zone under the hole over time. Reprinted with permission from Ref. [163] (Copyright 2008 American Chemical Society).

In [173], a rod was used as an obstacle locally blocking evaporation above the thin film surface (Fig. 7a). Nonuniform evaporation resulted in the appearance of a dip under the obstacle surrounded by a rim (Fig. 7b). The diameter of the rim corresponds to the diameter of the cylindrical rod. The experiment used a glass substrate and colloidal silica particles with a radius of about 11 nm. The rod radius  $R$  and the gap  $H$  between the rod and the film were varied in the experiment [173]. These two key parameters allow adjusting the width and depth of the dip. The liquid–air interface is curved in the process of nonuniform evaporation [173]. It becomes convex under the obstacle. The solid dried layer starts forming at a distance from the rod lo-

cation. The solid–liquid phase boundary gradually propagates toward the rod. The liquid flows from the closed area to the open area where evaporation is intense. In addition, the liquid is pumped out of the closed area by filtration. The resulting porous structure of the solid layer sucks the liquid into the capillaries because of the pressure gradient. The area of film under the rod dries last.

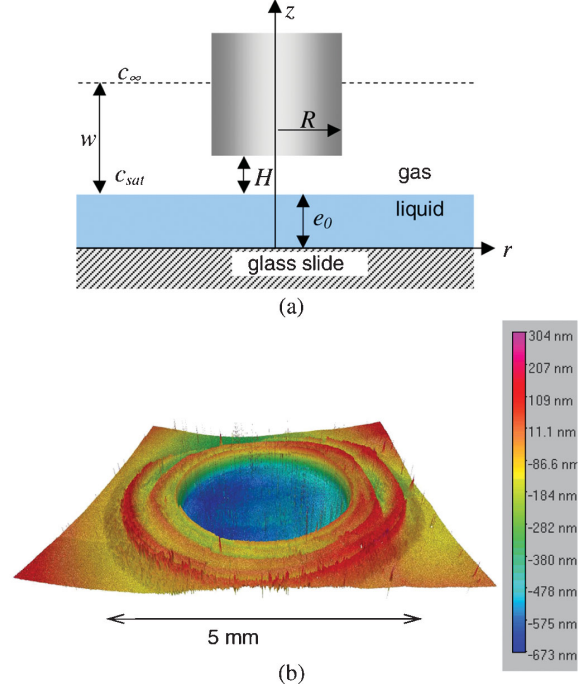


Figure 7: (a) Setup for film evaporation control: the film is schematically shown at the initial moment. (b) A dip with a rim is formed under the obstacle: the profile of the dried layer obtained with a film thickness  $e_0 = 3.5$   $\mu$ m, rod diameter  $2R = 5$  mm, and a gap  $H = 1$  mm observed using an optical profilometer (zero of the vertical axis corresponds to the film level away from the obstacle). Reproduced with permission from Ref. [173] (Copyright 2010 by The American Physical Society).

IRAEL (infrared radiation-assisted evaporative lithography [161]) is a modification of the approach proposed in [143] with a mask. To increase the evaporation rate, an infrared lamp is added to the system (Fig. 8) [161, 164]. If the melting point of polymer particles exceeds room temperature, then external IR heating enables the coalescence of particles. A relief glass film without cracks is formed after drying. For comparison, structures of solid polymer particles obtained using the standard method [143] are brittle. The thickness of thin solid films with a stable periodic structure can vary from several microns to submillimeter sizes [161, 164]. In [143], the evaporation process lasted about two hours because the mask blocks a part of the free film surface. In the case of IR heating, the process lasts several minutes or dozens of minutes depending on the lamp power [161, 164]. High-power lamps should be used in a way that avoids overheating the system. The issue is that a boiling liquid adversely affects the formation of the required pattern [164]. The radiation power density is  $P_d = P_E/(2\pi r_l L)$  [161] or  $P_d = P_L/(4\pi r_l^2)$  [164], where  $r_l$  is the distance from the film surface to a light source,  $L$  is the length



of a cylindrical emitter,  $P_E$  and  $P_L$  are the respective emitter and lamp powers.

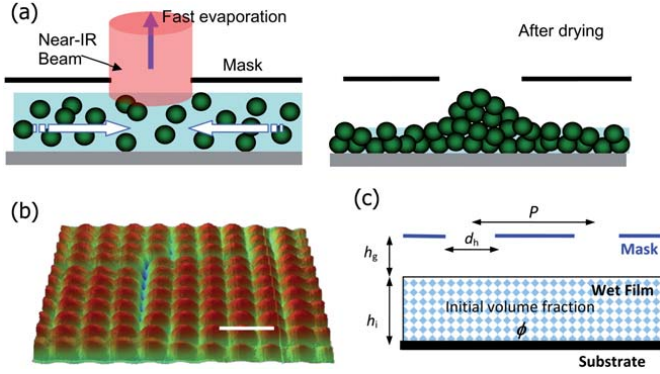


Figure 8: (a) A film evaporating under a mask illuminated by an IR lamp; (b) the resulting pattern (scale bar is 3 mm); (c) physical parameters of the system. Reproduced from Ref. [161] with permission from The Royal Society of Chemistry.

The authors of [161] used aqueous latex films and an IR lamp ( $P_L = 250$  W) in their experiment to study the influence of  $h_i$ ,  $\phi_i$ ,  $h_g/P$ , and  $P$  on  $\Delta h$ . The value of  $\Delta h$  linearly increases as the initial film height  $h_i$  increases. The vertical distance between the peak and the valley  $\Delta h$  also increases with pitch  $P$ . This only occurs until a certain value ( $P \approx 3$  mm) is achieved. Further increase in  $P$  does not affect the increase in  $\Delta h$ . An increase in the initial volume fraction  $\phi_i$  causes an increase in  $\Delta h$  if  $\phi_i < \phi_c$ . The value of  $\Delta h$  decreases if the initial volume fraction is above a critical value of  $\phi_c \approx 0.35$ . A decrease of  $\Delta h$  is also observed when  $h_g/P$  is increased.

Marangoni flow in IRAEL is expected to be directed from open areas to those covered with a mask having relatively cold temperatures, but the authors [161] observed an accumulation of substance in the open areas. This indicates that the compensatory flow resulting from evaporation dominates. For a theoretical estimate, they used a characteristic thermocapillary flow velocity  $V_M = (h_i/L)(d\gamma/dT)(\Delta T/\mu)$  and a typical compensatory flow velocity  $V_E = LE/h_i$ , where the capillary length is  $L = h_i(\gamma/(3\mu E))^{1/4}$ ,  $\gamma$  is the surface tension,  $\mu$  is the solution viscosity,  $E$  is the evaporation rate, and  $\Delta T$  is the temperature gradient. With a high ratio of  $\psi = V_M/V_E$ , Marangoni flow prevails. The compensatory flow prevails when  $\psi$  is low. As the volatile substance is lost, the solution concentration  $\phi$  grows along with the viscosity  $\mu(\phi)$ . As  $\mu$  increases,  $\psi$  decreases. This estimate thus confirms the observation of the fact that Marangoni flow disappears with  $\phi \geq 0.22$  [163].

The effect of IR emitter power on the system was studied in [164]. Carbon IR emitters with a power value from 1,600 W to 2,400 W were used in the experiment [164]. The radiation power density  $P_d$  was measured as a function of  $r_l$  and  $P_E$ . The value of  $P_d$  increases nonlinearly as the emitter power increases and the distance between the IR light source and the film decreases. With a higher power  $P_E$ , the temperature in the film rises faster over time. This allows adjusting the evaporation rate. Different substrate materials (brass, copper, steel, glass, paper, aluminum alloy, polyester) were used in [164]. The ex-

periment showed that the type of substrate material affects a parameter of the formed structure such as  $\Delta h$ . The difference in  $\Delta h$  is most likely due to the influence of heat conductivity, absorption of IR radiation by the substrate, and the surface energy of the material. To explain the empirical data obtained, more detailed research and mathematical modeling are needed.

There are several reasons for the deformation of the free surface of the liquid film, which plays an important role in evaporative lithography: surface disturbance by airflow, the edge effect in the three-phase boundary, partial covering of the film area with a plate, evaporation from an inhomogeneous substrate, etc. (Fig. 9). One of the promising directions is the use of composite substrates with variable heat properties [174, 175].

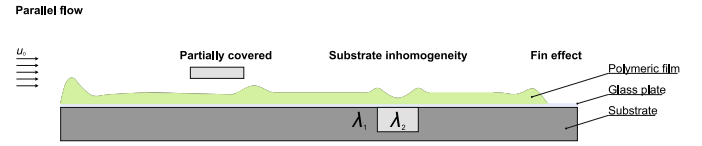


Figure 9: Possible causes of curvature of the liquid film free surface. Adopted from Ref. [175] with the permission of Springer.

An aluminum substrate with a Teflon strip applied was used in [174, 175]. The respective heat conductivity coefficients of aluminum and Teflon are  $\lambda_1$  and  $\lambda_2$  in Fig. 9. A thin glass plate with a liquid film was placed over the substrate. Such an approach allows using the substrate as a template many times because the pattern is formed on the glass plate. Teflon emits heat slower than aluminum because the latter has a relatively high heat conductivity. Therefore, the local part of the liquid film is relatively cold because of evaporation in the Teflon area. The aluminum substrate was placed in a drying channel through which air was blown. The airflow rate  $u$  was one of the parameters studied in [174]. Moreover, the experiment was conducted at different temperatures  $T$ . In the considered parameter ranges ( $u = 0.5\text{--}1.5$  m/s and  $T = 25\text{--}40^\circ\text{C}$ ), no significant differences in the final patterns of deposits were observed. A solution of methanol and polyvinylacetate was used [174, 175]. The surface tension of the solution was measured at different temperatures and concentrations [174]. The data on the dependence of the solution viscosity on concentration were also provided [175]. At different time stages of evaporation, several types of instability on the liquid surface were observed [174]. This is associated with the influence of the thermal and solutal Marangoni effects alternatively dominating in different process stages. A quasi-one-dimensional model was used in [174] to calculate the liquid mass fraction and the film surface temperature variation in time. According to the calculations, the temperature above Teflon is lower than that above aluminum. The mass fraction of liquid in the solution decreases faster above aluminum over time. Lateral mass and heat distribution were disregarded [174]. We do not discuss the model [174] in Sec. 3, because it is too simple.

In [175], the method with a composite substrate was compared with the film evaporation partially covered with a plate on top (Fig. 9). While the nonuniform evaporation in the first case is caused by the heterogeneous heat conductivity of the sub-



strate, the evaporation in the second method is simply blocked in a certain area by the plate. Figure 10 shows profiles of two final patterns obtained using these two methods. Both cases demonstrate a deposit peak in the part of the intensive evaporation area near the boundary of the slow evaporation area. The difference in the solid film thickness on a composite substrate was  $\Delta h \approx 20 \mu\text{m}$ . For comparison, in the pattern obtained due to partial blocking of evaporation with the plate,  $\Delta h \approx 55 \mu\text{m}$ .

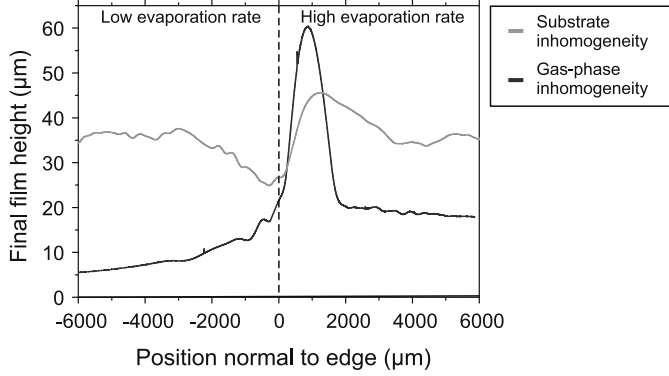


Figure 10: Comparison of profiles of the final patterns obtained using two methods. Reproduced from Ref. [175] with the permission of Springer.

The authors paid special attention to visualizing the flow and measuring its velocity [175], focusing on three areas: (1) center of the covered area, (2) the intermediate area, and (3) the open area. The maximum flow velocity was measured in the intermediate area,  $v_{\max} \approx 98 \pm 12 \mu\text{m/s}$ . The observation results showed that the flow velocity increases initially. After a while, the rate begins to decelerate because the solution viscosity increases as the solvent is lost. Details of the measurement method can be found in [176].

In some applications, the direction of the compensatory flow should be reversed to suppress the coffee-ring effect. In [177], the top central part of a droplet was heated by a  $\text{CO}_2$  laser. The droplet was placed on a hydrophobic substrate over a hydrophilic well. The well in the substrate corresponded to the droplet center. As a result of the heating, the evaporation rate in the central area was higher than in the periphery. Consequently, the compensatory flow was directed from the droplet periphery to its center. Over time, suspended DNA molecules accumulated in the well. At the same time, the three-phase boundary was displaced (“slip motion” or constant contact angle mode). Because the amount of DNA molecules in the periphery was small, no pinning occurred. After drying, stain-like deposits were formed. In contrast to the eOMA method [178] (see section 2.3), the method proposed in [177] does not require using surfactants.

An additional experiment with the heated substrate without using a laser was performed for comparison [177]. It was shown that in this case, a ring pattern formed in the area of the pinned three-phase boundary. The boundary was pinned because the DNA molecules accumulated, drifted by the compensatory flow toward the periphery where the evaporation rate was higher.

In contrast to the results in [177], during point heating of the droplet center with IR light, particles were carried with the flow

toward the periphery in the experiment in [179]. And when the point area at the droplet edge was heated, particles were carried to the opposite edge. The authors [179] explained this transfer by an emerging Marangoni flow. This flow is directed along the surface from a warm area to a cold area where liquid surface tension is relatively high. To confirm this, the authors [179] developed a mathematical model and performed a series of calculations. The model [179] describes buoyancy-induced flow and Marangoni convection in a constant droplet volume with heating of a surface point. The model [179] does not account for the convection–diffusion equation to describe the particles transfer nor does it account for the movement of the two-phase boundary or for volume heat flux resulting from the IR light passing through the liquid. The numerical results are difficult to attribute to evaporative lithography unlike the experimental part. Therefore, we do not describe the model [179] in detail in Sec. 3. For a pure water droplet, an influence of local heating both on Marangoni flows inside the drop and on the evaporation kinetics was observed in [180].

In summary, passive methods in evaporative lithography are usually based on controlling the geometric characteristics of the system [142, 143, 173], the heating temperature [161, 164, 177], and the physical and chemical properties of the liquid [171] and the substrate [174]. These methods are clear and easy to implement and can be used in several practical applications (see Sec. 2.4).

## 2.2. Active methods for controlling particle sedimentation

Real-time control of particle deposition using active methods is mainly achieved by regulating key dynamic parameters of the system. As a rule, this implies some kind of external influence, for example, a powerful light emitter [181] or an intensive air flow [182]. Parameters of external sources can be controlled during the drying of the colloidal liquid. In this section, we review the main experimental achievements regarding active methods in evaporative lithography.

The vapor concentration above the film surface can be controlled by a dry air flow. For example, a concentric nozzle was placed above a liquid film containing nanoparticles. This film was preapplied to a glass substrate [182]. Figure 11(b) shows the sketch of the experimental setup. A nozzle with two holes was used in [182], but more holes could be made (Fig. 11(a)). Dry air was blown out through the inner needle (inner radius  $R_1 = 0.25 \text{ mm}$ , outer radius  $R_2 = 0.42 \text{ mm}$ ). Air together with vapor was pumped in through the outer needle (inner radius  $R_3 = 0.69 \text{ mm}$ , outer radius  $R_4 = 0.92 \text{ mm}$ ). The dynamic parameter in such a system is the air flow velocity  $u$ . The maximum velocity of the blown-out airflow can be expressed as  $u_{\max} = 2Q/(\pi R_1^2)$ , where  $Q$  is the flow rate. If  $Q = 1 \text{ mL/min}$ , then we obtain the value  $u_{\max} = 0.16 \text{ m/s}$ . As a result of the experiment [182], dry deposition was obtained under the central part of the nozzle. The spot pattern diameter was approximately 1 mm (Fig. 11(c)). A series of experiments with different values of  $Q$  allowed determining the dependence of the dry spot diameter and height on the air flow velocity. As  $Q$  increases, the diameter decreases, and the height increases [182]. In addi-

tion, the authors [182] also developed a mathematical model of this experiment (see Sec. 3).

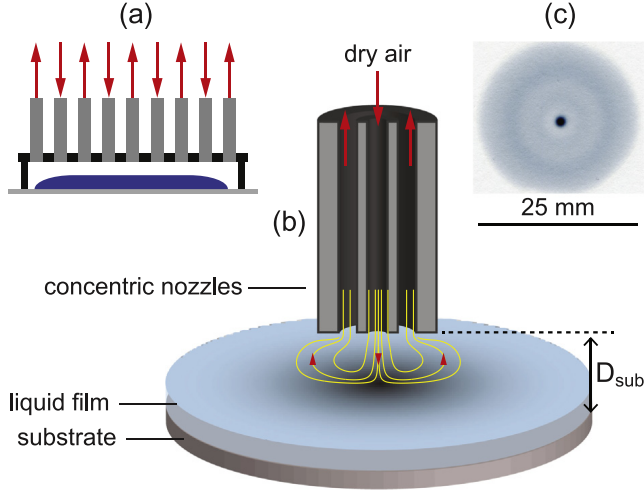


Figure 11: (a) Active control in evaporative lithography schematically. (b) Sketch of the experimental setup. (c) Image of the resulting pattern. Reprinted from Ref. [182]. Copyright 2018 with permission from Elsevier.

Infrared (IR) beams can be projected to the solution surface without a mask. For this, an IR laser and a digital multimiror device were used in [181]. The authors presented the proposed technology as an active method for controlling the deposition of the substance during evaporation, suitable for use in the production of organic electronic materials. Such a system allows engineers to realize both time-based modulation of illumination intensity and spatial modulation very rapidly in a parallel manner. Two different types of solutions were used in the experiment in [181]. (1) An aqueous dispersion of poly(3,4-ethylene dioxythiophene)-poly(styrene sulfonate) (PEDOT:PSS) was taken as a high-molecular-weight solution. (2) A low-molecular-weight solution was also used that included red and blue light-emitting polymers dissolved in mesitylene. For the first type of solution, the initial film thickness was  $h_0 \approx 160 \mu\text{m}$ . For the second type of solution, the film was relatively thin,  $h_0 \approx 1$  to  $3 \mu\text{m}$ . The experimental results showed two process behaviors depending primarily on the film thickness and molecular weight of the dissolved substance. The dissolved high-molecular-weight substances, which form a skin on the free surface of relatively thick films, tend to accumulate in irradiated areas where the evaporation rate is highest. In contrast, the redistribution of low-molecular-weight dissolved substances in thin films is caused by the surface tension gradient resulting from temperature and concentration differences, which can lead to a decrease in the dissolved substance in the illuminated areas. In other words, an inverted pattern is obtained. Figures 12a and 12c show the light templates (white color shows illuminated areas). The corresponding patterns are shown in Figs. 12b and 12d. To obtain a text from a red light-emitting polymer (figure 12b), the experimenters [181] applied an inverted light template (figure 12a). The thickness of the PEDOT:PSS dried layer was several microns (figure 12d). A numerical simulation of this experiment was performed in [181]

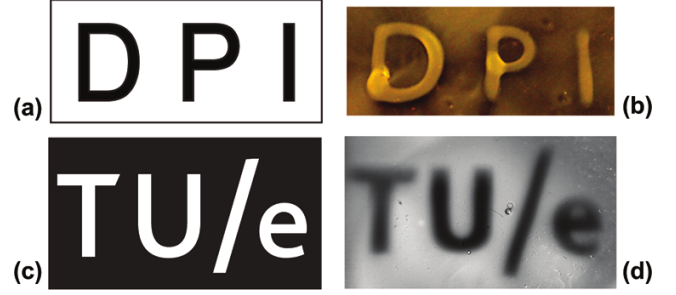


Figure 12: (a, c) IR light templates and (b, d) corresponding modulated deposition patterns for (b) the dried solution of mesitylene and the red light-emitting polymer (pattern width is 2 cm) and (d) PEDOT:PSS in water (pattern width is 2.5 cm). Reprinted with permission from Ref. [181]. Copyright 2012 American Chemical Society.

(see Sec. 3). Further studies in this field will allow optimizing the proposed method.

Marangoni flow can also be controlled in real time by a point vapor source. Changing the location of the vapor source above the droplet in space and time was proposed in [183] to achieve the structuring of deposits on the substrate. The source was a needle with inner diameter of  $r_0 \approx 80$  to  $640 \mu\text{m}$ . Dry ethanol was used as vapor. We let  $\gamma_1$  denote the liquid surface tension near the periphery. In the vapor source area, the surface tension reduces to  $\gamma_2$  ( $\gamma_1 > \gamma_2$ ). The surface tension gradient causes the emergence of Marangoni flow that redirects the transfer of suspended particles. In the absence of ethanol, the capillary flow forms an annular pattern. In the presence of a vapor source (dry ethanol), the Marangoni flow arises, and a central spot is formed.

In the experiment in [183],  $1 \mu\text{L}$  droplets with silica particles of about  $2 \mu\text{m}$  (density of  $\rho_{\text{Si}} = 1850 \text{ kg/m}^3$  and the sedimentation rate in water of  $v_s \approx 2.1 \mu\text{m/s}$ ) were used. The droplet contact angle on glass is  $\theta \leq 5^\circ$ . Measurements showed that the flow velocity increases as  $h$  decreases ( $h$  is the distance from the substrate to needle tip). If  $h$  is low, then the flow velocity  $v$  exceeds the sedimentation rate  $v_s$  by more than an order of magnitude. The authors [183] obtained an analytic estimate,

$$v(h) = \frac{h_D}{2\eta R} [\gamma(h, R) - \gamma(h, 0)],$$

where  $\eta$  is the water viscosity,  $h_D$  is the droplet height and

$$\gamma(h, r) = \gamma_w - \frac{\beta}{2} \frac{c_0 r_0}{\sqrt{(h - h_D)^2 + r^2}}.$$

Here,  $c_0$  is the ethanol concentration at the needle tip, and  $\beta$  is the proportionality constant [183].

As the vapor source is moved along the droplet surface, the location of the minimum surface tension can be dynamically shifted. This allows changing the flow configuration in the mode close to real time. Figure 13 shows several resulting patterns corresponding to different needle motion types.

Two years earlier, other researches achieved a similar result by displacing a substrate with droplet relative to a fixed laser

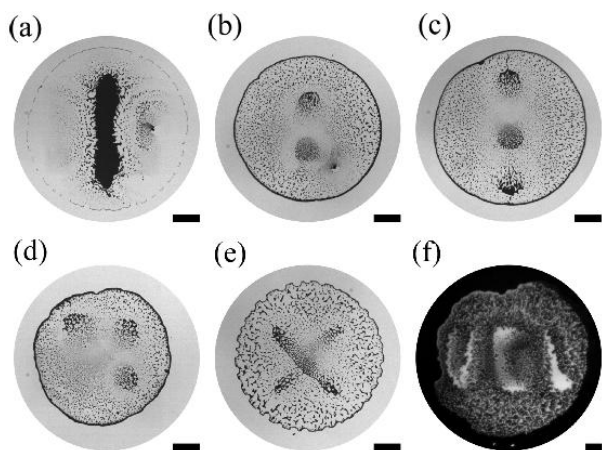


Figure 13: Applying a pattern to the surface using dynamic spatial and temporal control of the Marangoni flow. Different surface structures of deposited colloidal particles after evaporation obtained by shifting an ethanol vapor source in (a–c) one or (d–f) two spatial directions over time: (a) line, (b) two dots, (c) three dots in a line, (d) three dots in a 2D configuration, (e) cross, and (f) letters UCL. Scale lines correspond to 1 mm. Reprinted with permission from Refs. [183]. Copyright 2018 American Chemical Society.

emitter [184] (Fig. 14). The locally heated area loses its liquid due to evaporation relatively faster. Consequently, the compensatory flow rushes into the illuminated area, capturing and carrying the particles there. An IR laser with a wavelength of  $2.9\mu\text{m}$  was chosen for the experiment because water adsorbs the heat of the passing light wave well in this range. Polystyrene particles of about  $0.5\mu\text{m}$  in size were used. The authors [184] measured the dependence of the evaporation time of droplets on the radiation power density ( $53$  to  $224\text{ W/cm}^2$ ) for droplets of  $2$  to  $10\mu\text{L}$ . The size of the formed deposits was also measured as a function of the beam diameter. The types of deposits were also defined for the cases when the laser switches off at some point of time  $t_{\text{off}} \leq t_{\text{FL}}$ , where  $t_{\text{FL}}$  is the time of the complete drying of the droplet. The time intervals can be conventionally divided into three zones: (1)  $t_{\text{off}}/t_{\text{FL}} < 0.6$ , (2)  $0.6 \leq t_{\text{off}}/t_{\text{FL}} \leq 0.7$ , and (3)  $0.7 < t_{\text{off}}/t_{\text{FL}} \leq 1.0$ . Zone 1 corresponds to coffee-stain or coffee-stain-like structures. Uniform deposits are typical of zone 2. Inverted coffee stains were observed in zone 3.

The described active methods are preferred in terms of the broad ability to control the structure of the formed sediment, but they are still inferior in obtaining high-resolution patterns. These methods currently allow obtaining structures with a spatial frequency in the submillimeter and millimeter range. One possible way to solve this problem is to combine different approaches. Hybrid methods are discussed in detail in the next subsection.

### 2.3. Hybrid methods for controlling particle deposition

Hybrid methods combine flow control through evaporation with other approaches that are classified as EISA or not. Many variations are possible. Therefore, we do not try to mention all of them here but give only some illustrative examples.

Some applications require a uniform and relatively large deposit area of densely packed particles, for example, for the

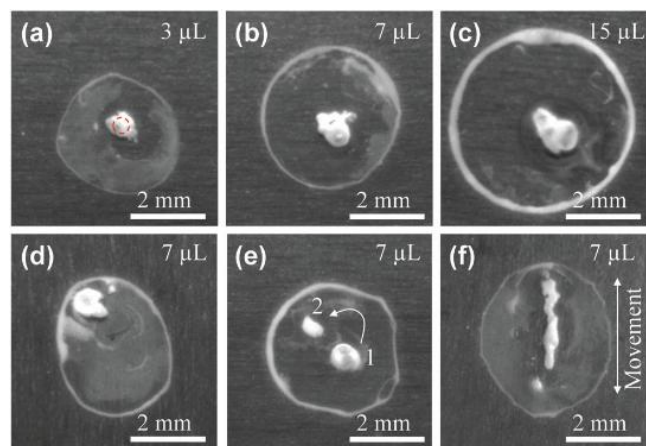


Figure 14: Particle deposit formation under exposure to laser beams under different conditions: (a–c) a laser beam is projected to the central part of a droplet; (d) a laser beam is projected near the periphery; (e) a laser beam is projected first to point 1 and after some time to point 2; (f) the substrate was moved relatively to the laser beam with a constant speed of  $0.12\text{ mm/s}$ . Reproduced from Ref. [184] with permission from The Royal Society of Chemistry.

creation of photonic crystals. Uniform deposit was obtained in [185] after directional evaporation from a Hele-Shaw cell. The colloidal film was in the gap between two glass plates. All sides except one were covered with varnish. Therefore, evaporation only occurred in the area of the open cell. The capillary flow carried the particles and arranged them into a multilayer structure toward the opening. The pattern formation was also affected by the capillary attraction of particles and their electrostatic interaction [185]. Weak diffusion was also observed in the system. It is noteworthy that densely packed and chaotic zones can be distinguished in the structure. Sometimes, cracks were observed in densely packed zones at the end of the process. Further study and more detailed knowledge of such processes will allow understanding ways to improve the properties of the resulting structure.

The method proposed in [186] is based on a combination of the compensatory flow directed toward the periphery and the optically induced Marangoni flow directed along the surface from the edge to the center. The experimental setup is shown schematically in Fig. 15a. The authors [186] used photosensitive surfactants AzoTab, which increased the water surface tension under ultraviolet (UV) radiation. As a result, the circulating flow carried colloidal particles into the central area affected by the UV light (Fig. 15b). This method was called evaporative optical Marangoni assembly (eOMA). In Fig. 15b,  $\gamma_{\text{UV}}$  and  $\gamma_{\text{vis}}$  are the respective surface tension factors under exposure to UV and visible light ( $\gamma_{\text{UV}} > \gamma_{\text{vis}}$ ).

Figure 16 shows examples of patterns formed by UV illumination of some areas of the droplet surfaces during evaporation, including the use of photo masks with different geometries (points, stripes, circles, squares, and letters). The droplet volume varied between  $12$  and  $20\mu\text{L}$ . The authors [186] are confident about the flexibility of this method. Their experiments proved the applicability of eOMA to different sizes and charges



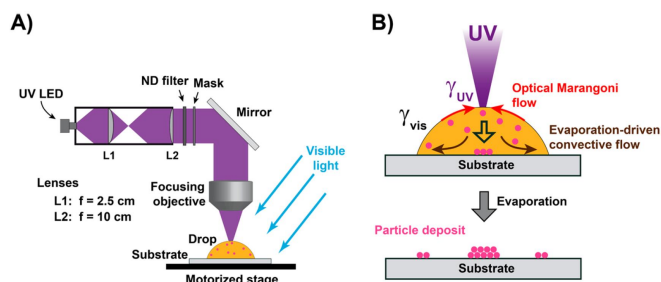


Figure 15: (a) Sketch of the experiment, (b) flow structure under the UV illumination of the central part of the colloidal droplet surface with additives of photosensitive surfactants; deposit type after drying. Reprinted with permission from Ref. [186]. Copyright 2015 American Chemical Society.

of particles.

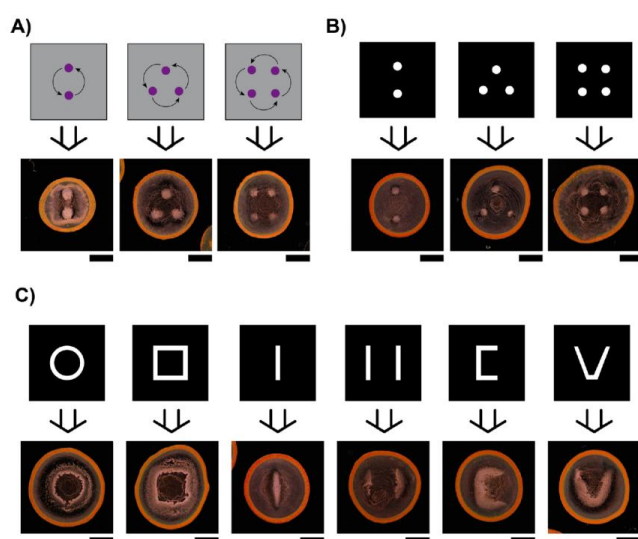


Figure 16: Patterns obtained using the eOMA method. (A) Single-spot scanning, (B) single-spots projected through photomasks, (C) strips, circles, squares, and letters projected through photomasks (scale lines correspond to 2 mm). Reprinted with permission from Ref. [186]. Copyright 2015 American Chemical Society.

Key parameters of the eOMA method were studied in detail in the subsequent work [178]. The authors considered the case where a thin (relative to the droplet base diameter) UV beam was directed to the central part of the droplet. This allowed obtaining a cylinder-shaped deposit in the middle of the ring. The following parameters were studied: the concentration of surfactants and colloidal nanoparticles and the diameter and intensity of the light beam. These parameters affect the size and volume of light-induced central particle deposit. In the experiment,  $7\ \mu\text{L}$  drops were used. The radius of central deposits varied from 0.1 to 0.7 mm at different values of the key parameters. Their height varied from 0.5 to  $1\ \mu\text{m}$ . The volume varied in the range between 0.05 and 0.3 nL. The Marangoni flow velocity was assessed based on the formula  $U_{\text{Ma}} \approx (h/\eta) \cdot \nabla\gamma$ , where  $h$  is the droplet height,  $\eta$  is the dynamic viscosity, and  $\nabla\gamma = \gamma_{\text{UV}} - \gamma_{\text{vis}}$ . The value of  $\nabla\gamma$  varied in the range of approximately 1 to 12 mN/m depending on the concentration of

surfactants. Measurements showed that the volume of central deposit increases nonlinearly with increasing colloidal nanoparticle concentrations. The size of the particles in the experiment was about 30 nm. The experiment also showed the possibility of forming a cylindrical deposit in an arbitrary area illuminated by a UV beam. The authors [178] determined the optimum surfactant concentration relative to the value of  $\nabla\gamma$  varying over time. It is better to have an initial concentration of  $C_s \ll \text{CMC}$ , where CMC is the critical micellar concentration. Then during most of the process time,  $\nabla\gamma$  takes a relatively high value.

Another method combines evaporative lithography and topographic and chemical surface modification. A method was developed in [187] based on using evaporative lithography in open microfluidic channel networks (Fig. 17a). First, a solid surface was topographically structured using a photolithography method based on polydimethylpolysiloxane (PDMS photolithography). For the experiment, several substrates with different channel geometries were manufactured: straight, zigzag, and square mesh. Channel widths varied between 5 and  $10\ \mu\text{m}$ , and the depth was about  $5.6\ \mu\text{m}$ . The microchannels were connected to a loading reservoir (a cell in the form of a cavity in the substrate to locate the droplets). Such a system of cavities in the substrate was subject to plasma treatment. Hence, the surface wetting property in these areas changed locally from hydrophobic to hydrophilic. The multilayer particle structure was obtained in three stages (Fig. 17b): (1) Liquid flows quickly through hydrophilic microchannels after colloidal droplets are placed in the reservoir. (2) The flow generated by evaporation carries the particles toward the dead end of the channel. (3) The formed deposit boundary slowly moves from the dead end of the channel toward the reservoir.

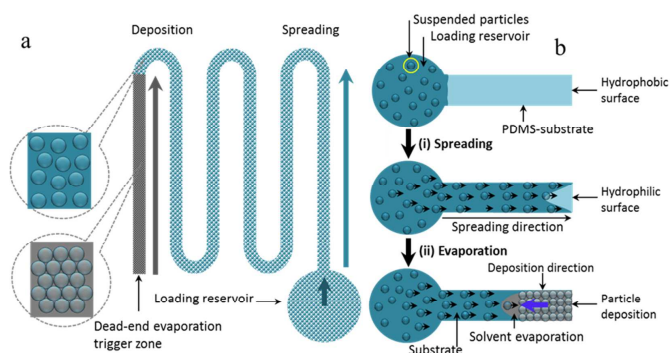


Figure 17: (a) Schematic diagram of the experiment [187] with the evaporation of liquid from open microchannels. (b) Three main process stages. Reprinted with permission from Ref. [187]. Copyright 2017 American Chemical Society.

Micro- and nanoparticles were used in the experiments [187]. The proposed method will allow for the future production of thin transparent electric conductive films with the required width of the conductor and the required gap between adjacent layers. Further development of this approach can involve its application to polymers, pigments, vesicles, cells, bacteria, viruses, and other biological molecules to build 2D and 3D structures. Additional studies are required in this field.

Another experiment showed the possibility of forming polygonal deposits when a colloidal droplet dries on a microstruc-

tured substrate [188]. Soft lithography followed by etching was used to fabricate such a substrate with an array of micropillars (Fig. 18a). The droplet volume in the experiment [188] was about  $2\mu\text{L}$ . Polystyrene particles of different diameters were used (0.1, 0.5, 1.0, 10,  $20\mu\text{m}$ ). Structures with a different pitch between the pillars (30, 90, 120,  $140\mu\text{m}$ ) were used with fixed values of the pillar diameter ( $30\mu\text{m}$ ) and height ( $100\mu\text{m}$ ). We note that the structured deposits obtained using this method contained no cracks (Fig. 18b,c), which is important for inkjet printing, for example. The phenomenon of hexagonal pattern formation requires clarification, and this issue remains open [188].

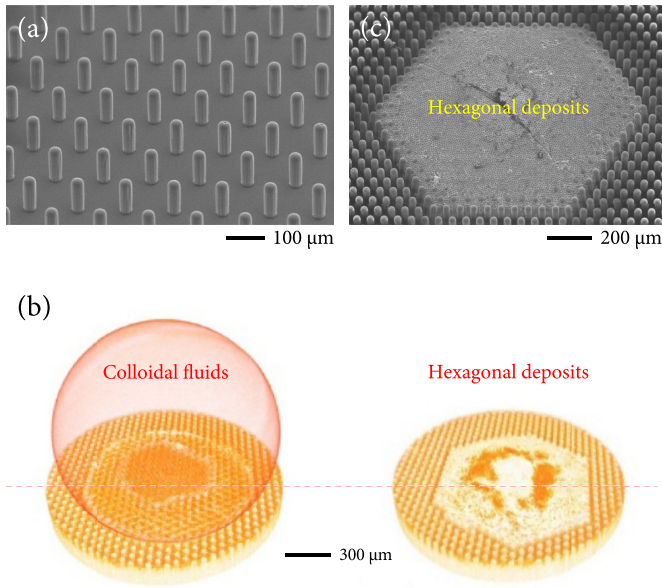


Figure 18: Hexagonal deposits: (a) Image of a hexagonal array of micropillars (scanning electron microscopy). (b) Restored x-ray tomographic images of colloidal liquid on a hexagonal array of micropillars (left) and hexagonal deposit after evaporation (right). (c) Image (scanning electron microscopy) of the hexagonal deposit on a hexagonal array of micropillars. Reproduced with permission from Ref. [188] (Copyright 2019 by The American Physical Society).

A combination of colloidal bead self-assembly and evaporative lithography was proposed in [189]. A liquid with gold nanoparticles (approximately 20 nm in diameter) was added to a monolayer of densely packed polystyrene microspheres (50 or  $100\mu\text{m}$  in size) on the substrate. As a result, a network of liquid bridges formed in the cavities between the microspheres. Packing of particles can be controlled by adding a surfactant to the solution [190]. The mechanism of stabilizing the liquid bridges was studied in [191]. After the microspheres are removed with adhesive tape, the network remains on the substrate. During slow evaporation, nanoparticles do not drift to the contact line because diffusion prevails over convection. After evaporative assembly, microwire patterns are formed from nanoparticles. The width of the individual wires ranges approximately between 2 and  $4\mu\text{m}$ . Their height is about 1 to  $2\mu\text{m}$ . The authors called this method “bridging lithography” [189]. The resulting network structure can be used as a transparent conductive coating. Measurements showed transparency exceeding 80% and

resistance per square from 0.5 to  $1.0\Omega/\square$  [189]. A mask template placed on the substrate made using the photolithography method can be used instead of microspheres [192]. To obtain quantum dots in the form of nanorings, a combination of colloidal lithography and capillary lithography can be used [193]. This method was called “evaporative templating.” In the drying film, microspheres are formed as a monolayer on the substrate. Nanoparticles occupy the pores between these spheres. In the process of evaporation, nanoparticles are attracted to the microspheres by capillary action. The latter are in turn removed from the surface. As a result, many individual nanorings with a diameter varying from a few nanometers to several hundred nanometers remain on the substrate [193]. The authors of [194] proposed to combine die-coating technology, an EISA method based on a capillary bridge (stick-slip motion of contact line), and active evaporation control due to local air flow.

Hybrid methods can be both active and passive (Fig. 1). Development in this direction can be associated with combining other effects with evaporative lithography. In particular, the transfer of particles can be affected by an electrowetting effect [195], magnetic [196, 197, 198, 199] and acoustic [200] waves, gravity [201] and centrifugal force (spin coating) [202, 203], porous substrate imbibition [204, 199], salt additives [205, 206, 207], etc. The emergence of new methods and the wide interest in evaporative lithography are due to a large number of relevant applications in various fields of human activity.

#### 2.4. Evaporative lithography applications

Such promising applications as the formation of transparent and conductive structures for the purpose of optical electronics and microelectronics [187, 189, 208, 209], mass transfer in nanoliter cells applicable to labs-on-a-chip [171], and polygonal deposits without cracks for inkjet printing [188] have already been mentioned above. We now consider the prospects of applying evaporative lithography in various areas in detail.

One of the promising directions in micro- and optoelectronics is the use of organic materials. For example, organic transistors are created by drying droplets with crystals after application on a dielectric substrate by an inkjet printing method [210]. Active control over deposition in an evaporating solution using infrared radiation can be used in an organic light-emitting diode (OLED) creation process [181]. Sediment formation in a drying droplet is one possible approach for producing P-OLED (polymer-organic light-emitting diode) [211] and QLED (quantum dot light-emitting diode) displays [193, 212, 213]. Another promising application in optical electronics is the creation of flexible thin-film photovoltaic elements [214]. A modification of EISA with a tilted movable substrate was used in [214] to obtain cyclic thin films of perovskite nanowires.

A transparent conductive structure was obtained in [215], where an inkjet printing process was used to form an array of droplets on a substrate. After the droplets dried, the substrate was left with an array of ring deposits. The procedure was repeated several times. Water ink with a silver nanoparticle content of about 0.5% of the solution weight was used. The particle

diameter was about 5–20 nm. The resulting patterns of overlapping rings are characterized by good transparency (95%) and resistance per square (specific resistance of  $0.5 \text{ cm}^2$  is approximately  $4 \Omega/\square$ ). The ring had a width of about  $10 \mu\text{m}$ , a height of about  $300 \text{ nm}$ , and a diameter of about  $150 \mu\text{m}$ .

This technology was later applied to carbon nanotubes, which are a good alternative to traditional materials (metal oxides) for optoelectronic devices [216]. In [217], liquid droplets were applied to a metal mesh placed over a plastic substrate. After drying, the metal mesh was removed. A mesh-shaped deposit of silver nanoparticles remained on the substrate. After the chemical sintering of the particles by HCl vapor treatment at room temperature, a transparent electrically conductive flexible film was obtained [217]. Silver nanowire structures were also obtained in [218].

Plasmonic metamaterials can be manufactured using the IRAEL method [219, 220]. A mask and an IR lamp were used in [219]. After the polymer solution with gold nanoparticles (10 nm in diameter) dried, a textured glass layer was formed (Fig. 19). In the resulting solid film, nanoparticles were concentrated in convex areas of the polymer that formed under the holes in the mask. Different sizes of polymer particles (160, 280, 400 nm) were used in the experiment [219]. The proposed approach to organizing inorganic nanoparticles in a polymeric coating is one-step and suitable for regulating optical properties on a macroscale with a period of several millimeters. By reducing the size of the polymer particles, this technology can also be used to obtain structures whose optical properties change with a period of about 10 microns.

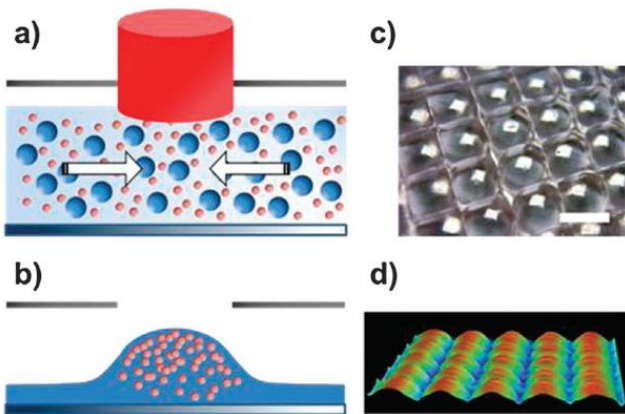


Figure 19: Schematic illustration of the IRAEL process: (a) Solution of polymeric acrylic particles (blue) and gold nanoparticles (red). (b) Polymeric particles sinter and form a solid coating containing gold nanoparticles. (c) Photograph of a solid film with periodic properties (scale 2 mm). (d) Three-dimensional surface profilometry. Reproduced from Ref. [219] with permission from The Royal Society of Chemistry.

In [220], a 2D plasmonic structure of gold nanoparticles was obtained on the surface of a 3D photonic crystal without using a mask. The authors [220] constructed a model based on the Langevin equation to describe Brownian particle dynamics. The LAMMPS library was used in the calculations. Polymeric particles on the liquid free surface play the role of a template. Rapid evaporation under light heating results in an accumula-

tion of particles near the two-phase liquid–air boundary. This is the case when the Peclet number  $Pe_{\text{evap}} > 1$  ( $Pe_{\text{evap}} = HE/D_s$ ,  $E$  is the free boundary movement velocity during evaporation,  $D_s$  is the particle diffusion coefficient, and  $H$  is the initial film thickness). The process takes about seven minutes. As a result of diffusion, gold nanoparticles are arranged in voids between polymer particles (338 nm in diameter) near a free surface. This approach allows for obtaining periodic nano- and microscale patterns in a short time.

Superlattices of structured iron oxide nanospheres coated with oleic acid can also be obtained by evaporating droplets on a silicon wafer [196]. In experiments [196, 221], the evaporation rate was controlled by placing the wafer with a droplet inside a special cell. Moreover, particles were additionally exposed to a weak magnetic field [196]. In [221], a staircase superstructure of nanocuboids (golden core coated with silver enclosure) was obtained in a ring-shaped deposit.

The formation of the deposit pattern can be used to diagnose diseases in health care. For example, a simple, low-cost method based on the disturbance of the coffee-ring pattern by a biomarker was described in [11], where this diagnostic method was tested in an example application of diagnosing malaria. In the experiment, the biological sample was mixed with a solution containing three kinds of particles. Of these, the surface of two kinds of particles is able to interact with the biomarker of the disease. These are magnetic particles (grey) and biomarker indicator particles (green). The third type is inert particles (red). Biomarkers in the solution bind the surfaces of functionalized particles (magnetic and indicators). Gray particles are deposited in the central part due to the magnetic field (Fig. 20). The flow of liquid carries the red particles to the periphery of the drying droplet. In the absence of a biomarker, the green particles are also carried to the forming ring deposit. The combination of red and green particles gives the ring a yellow color, indicating a negative test result. If the result is positive, the ring color is red. In addition, the central spot inside the ring becomes green as the indicators are deposited together with magnetic particles. Such structures are easy to interpret.

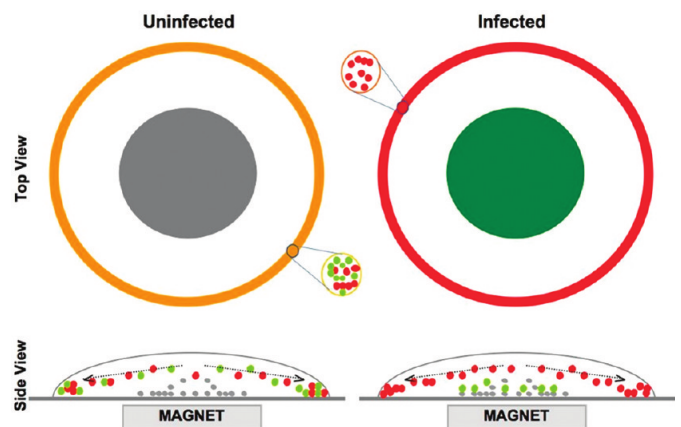


Figure 20: Coffee ring assay schematic. Reprinted with permission from Ref. [11]. Copyright 2011 American Chemical Society.

Another method based on the coffee ring effect allows detect-



ing protein molecules (e.g., thrombin) in a sample [222]. One more application in health care is the formation of microneedles on a plate for local safe and painless intracutaneous injections of drugs [223, 224]. We also mention biosensors used in environment and food safety analysis [225].

Localized fluid inclusions provide solid materials with multiple functions such as self-recovery, secretion, and controlled mechanical properties in a spatially controlled mode. An experiment [162] suggested a method for selectively localizing liquid drops in a supramolecular gel obtained from the solution using evaporative lithography (Fig. 21). The formation of areas saturated with suspended droplets occurs in the free evaporation area where the nonvolatile liquid is concentrated. The phases are thus separated before gel formation. A homogeneous gel matrix forms in the areas with hindered evaporation. The subareas underneath the mask openings and in the closed areas were characterized by different functional properties: slipperiness, self-healing, transparency, etc. [162]. There is no mathematical description of the process in [162], and the schematic legend of Fig. 21 therefore raises additional questions. For example, how does the compensatory flow transfer relate to the redistribution of the substance by the solutal Marangoni flow? Analytic estimates and mathematical modeling will allow further understanding of the mechanisms of this process in more detail. We discuss the current state of development of mathematical models of processes related to evaporative lithography in Sec. 3.

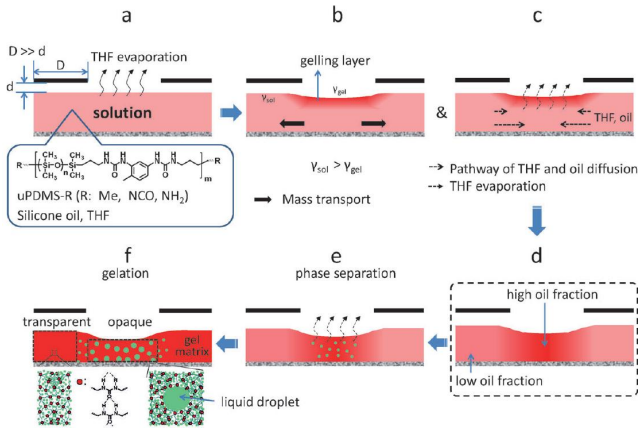


Figure 21: Control of localization of liquid droplets in a gel matrix using evaporative lithography: (a) A homogeneous solution consisting of copolymer, silicone oil, and volatile tetrahydrofuran. The solution film is applied to a flat substrate and covered with a mask on top. (b) The volatile liquid evaporates rapidly in open areas resulting in a surface tension gradient and hence mass transfer from open to closed areas. (c) Tetrahydrofuran diffuses from closed to open areas as does oil. (d) Nonuniform distribution of silicone oil. (e) Phase separation due to excess oil in open areas resulting in formation of silicone droplets. (f) Gelation and formation of a structured coating. Reproduced with permission from Ref. [162], Copyright 2016 WILEY-VCH Verlag GmbH & Co. KGaA.

## 2.5. Dimensionless parameters in evaporative lithography

When studying heat and mass transfer processes, dimensionless parameters controlling the nature of these processes are of

natural interest (see e.g. [226]). For physical processes occurring in evaporating sessile droplets, there are additional dimensionless characteristics whose effect is very significant. The many parameters whose roles were analyzed in this respect in [9] include the Bond number, the buoyancy number, the ratio of substrate to fluid thermal conductivities, and many others. We present the main dimensionless parameters additionally arising in evaporative lithography problems in Table 1.

The complex structure of boundaries arising in such problems produces a large number of geometric dimensionless parameters that affect the experimental outcome. As already discussed in Sec. 2.1, an increasing  $h_g/P$  ratio leads to a decrease in  $\Delta h$  [143, 161]. Weak particle segregation is observed for  $h_g/P \geq 0.3$  (the value of  $\Delta h$  is small) [143]. The values of  $\phi$  determine the type of sediment (discrete elements in the masked sediment for  $\phi < 0.07$  or continuous textured sediment layer for  $\phi > 0.07$ ) [143]. The value of  $\Delta h$  depends on  $\phi$  nonlinearly. It begins to decrease for  $\phi > 0.35$  [161]. At a rather high  $\phi > 0.22$ , Marangoni flow can be suppressed [163]. The phase transition of the liquid film to the solid phase occurs for  $\phi \geq 0.64$  [143]. An increase of  $P/d_h$  causes an increase in distance between adjacent elements of sediments [143]. The diameter of the elements of nanoparticle sediments inside pores formed by microparticles corresponds to the size of a hole in the mask at  $a_\mu/a_{\text{nano}} \geq 7$  [172]. An increase of  $R/H$  leads to an increase in the evaporation rate gradient above the film in the rod area [173]. An adjacent droplet has no effect when the values of  $L_i/D_c$  are rather high. Conversely, the maximum effect of one droplet on the mass transfer process in another is observed as  $L_i/D_c \rightarrow 1$  [168]. An increase in  $D_{\text{beam}}/D_c$  results in an increase in sediment size relative to the drop size [184, 178]. Reducing the value of  $r_0/h$  reduces the spot sediment area until it completely disappears at  $r_0/h = 0.04$  [183]. At a relatively high value ( $r_0/h \approx 0.32$ ), the spot is strongly smeared over the contact area of the droplet with the substrate. Particle transfer to the irradiated area is more efficient for  $C_s/\text{CMC} \ll 1$  [178]. In this case, the surface tension difference  $\nabla\gamma = \nabla\gamma(C_s)$  takes relatively high values for most of the drop evaporation time, which leads to a strong Marangoni flow.

Parameters such as  $Pe$ ,  $Pe_{\text{evap}}$ , and  $\psi = V_M/V_E$  characterize heat and mass transfer processes in the liquid phase. For  $Pe \gg 1$ , flow transport dominates, which results in obtaining a structured sediment. For  $Pe < 1$ , diffusion transport dominates, which results in uniform sedimentation [182]. Skin formation occurs for  $Pe_{\text{evap}} \gg 1$  [220, 182, 227]. Marangoni flow prevails for  $\psi > 1$  [161]. In the case of small initial particle concentrations, this can lead to an inverted sediment structure [163]. If compensatory flow prevails ( $\psi < 1$ ), then the particles are transported into areas under holes in the mask.

The parameter  $\Delta J/J_{\text{free}}$  characterizes mass transfer in the air phase and affects the hydrodynamics. As it increases,  $\Delta h$  also increases [143]. Here,  $J_{\text{free}}$  is the vapor flux density above the film with no mask, and the difference between the vapor flux densities in an area closed with a mask and an open area (under a hole) is  $\Delta J = J_{\text{max}} - J_{\text{min}}$ . During exposure by air flow to evaporating film at Reynolds number values  $Re_{\text{air}} \gg 1$ , a dip may be observed in the film until a rupture occurs [182, 228].

Table 1: Dimensionless parameters in evaporative lithography

Dimensionless parameter	Definition	Typical values
$h_g/P$	Ratio of gap $h_g$ to pitch $P$	0–1.25
$\phi$	Initial volume fraction of particles	0–0.64
$P/d_h$	Ratio of pitch $P$ to hole diameter $d_h$	2–10
$\Delta J/J_{\text{free}}$	Ratio of vapor flux density difference $\Delta J$ to freely evaporating film vapor flux density $J_{\text{free}}$	0–10
$\text{Pe}_{\text{evap}} = HE/D_s$	Peclet number related to the evaporation-induced interface motion	$10^{-2}$ – $10^8$
$\psi = V_M/V_E$	Ratio of Marangoni flow velocity $V_M$ to compensatory flow velocity $V_E$	0.01–2000
$a_\mu/a_{\text{nano}}$	Ratio of microparticle radius $a_\mu$ to nanoparticle radius $a_{\text{nano}}$	2–1000
$R/H$	Ratio of rod radius $R$ to rod–film gap $H$	0.5–4
$L_i/D_c$	Ratio of interdroplet distance $L_i$ to contact diameter $D_c$	1– $\infty$
$D_{\text{beam}}/D_c$	Ratio of beam diameter $D_{\text{beam}}$ to droplet size $D_c$	0.12–0.22
$t_{\text{off}}/t_{\text{fL}}$	Ratio of irradiation time $t_{\text{off}}$ to evaporation time $t_{\text{fL}}$	0–1
$\text{Re}_{\text{air}} = \rho_{\text{air}} u_{\text{max}} R_1 / \mu_{\text{air}}$	Jet Reynolds number ( $\rho_{\text{air}}$ and $\mu_{\text{air}}$ are the air density and viscosity)	0–10
$\text{We} = \rho_{\text{air}} u_{\text{max}}^2 R_1 / \gamma$	Weber number ( $\gamma$ is the liquid surface tension)	0–1
$\text{Pe} = V_{\text{max}} R_1 / D_s$	Peclet number related to the lateral fluid flow ( $V_{\text{max}}$ is the lateral flow velocity)	$10^{-2}$ – $10^8$
$r_0/h$	Ratio of inner needle radius $r_0$ to needle–substrate distance $h$	0.04–0.32
$C_s/\text{CMC}$	Ratio of initial surfactant concentration $C_s$ to critical micellar concentration CMC	0–1

In such cases, particle transfer is no longer controlled by adjusting the vapor concentration above the free surface of the liquid. There are often several dry spots if the value of the Weber number is approximately unity or greater [228]. These parameters are restricted in evaporative lithography ( $\text{Re}_{\text{air}}$  near unity and  $\text{We} \ll 1$ ).

Parameters such as  $t_{\text{off}}/t_{\text{fL}}$  can also be relevant in an experiment. This parameter determines the portion of the process time controlled by external radiation. The rest of the time, the process occurs naturally (without external influences). Hence, the value of  $t_{\text{off}}/t_{\text{fL}}$  affects final sediment shape [184]. An annular sediment is observed for  $t_{\text{off}}/t_{\text{fL}} < 0.6$ . A value in the range from 0.6 to 0.7 results in a uniform sediment. Inverted deposition is obtained for  $t_{\text{off}}/t_{\text{fL}} > 0.7$ .

The listed parameters facilitate a comparative analysis of experiments for which they are important. For example, the mass transfer process depends on the main key parameter  $\Delta J/J_{\text{free}}$  in experiments with a mask [143] and with a composite substrate [174] (Sec. 2.1). In the case of a composite substrate,  $J_{\text{free}}$  corresponds to the vapor flux density in the area where the thermal properties of the substrate were not changed previously (Teflon coating, etc.). The parameter  $\Delta J/J_{\text{free}}$  can be expressed theoretically in terms of the ratio of thermal conductivities  $(\lambda_2 - \lambda_1)/\lambda_1$  (Fig. 9) for the experiment [174].

### 3. Mathematical modeling of heat and mass transfer in droplets and films under nonuniform evaporation

#### 3.1. Preliminary remarks

Although evaporative lithography has by now evolved as an independent field of research, the development of relevant applied methods and theoretical approaches has often been inextricably linked with the development of other studies of the evaporation of liquid layers and droplets. Some of the relevant studies are or may have been predecessors to this field, while others may be useful for its further development. We present a few examples.

The model in [229] describes the geometry of depositions during their formation in evaporating colloidal droplets on a flat substrate. Some assumptions of the model, such as independence of evaporation from free droplet surface from the availability of dissolved substances, were discussed by the author in detail. The transport of colloidal particles to the contact line in the case of an asymmetric evaporating colloidal droplet in which the contact line contains an acute angle was studied in [230] in the approximation of homogeneous evaporation. The formation of a structured sediment upon drying of a colloidal droplet was modeled in [231] with the effect of the capillary attraction of particles taken into account. Based on the simulations, the physical mechanisms of forming individual chains of particles inside an annular sediment were analyzed.

To describe the spatial distribution of colloidal particles and hydrodynamic flows in an evaporating sessile droplet and also the structure of the sediment after drying, the obtained experimental results were analyzed in [232] using numerical simulation based on the finite element method of the joint solution of the Navier–Stokes equations in a liquid, the heat conduction equation in the droplet and substrate, the equation of vapor diffusion in air, and the convection–diffusion equation to account for the transfer of particles in the droplet. A negligible influence of colloidal particles on fluid hydrodynamics was assumed, and an axisymmetric solution was considered (2D model). During evaporation, the solid phase area can propagate when the critical concentration of the solution achieves dense packing of the particles. The contact line becomes depinned when the wetting angle decreases below a certain value. In [233], electrostatic and van der Waals interactions between colloidal particles and the solid substrate were added to the model using DLVO theory. This leads to DLVO forces in the convection–diffusion equation. The DLVO interaction forces depend on the pH value of the solution, for which several different values were used. Depending on the parameter values, single-ring deposits, a homogeneous spot, or accumulation of particles in the center of the dried-up droplet were obtained as a result of the calculations [232, 233].

Periodic pinning and depinning of a moving contact line and formation of structured sediments on glass plates during evaporation in a vertical Hele–Shaw cell were studied experimentally and theoretically in [106, 107]. The obtained expression for the pinning force demonstrates that it is determined by the geometry of the growing sediments and the force of gravity.

A similar problem statement in which the meniscus of a thin film of a colloidal fluid is in contact with a moving substrate was considered in [234, 235]. For the computer simulation, the solution of the hydrodynamics and the dissolved substance transport were calculated in the framework of the lubrication approximation, and evaporation was also taken into account using the diffusion model. The influence of capillary forces on the meniscus shape was not accounted for in [234, 235], because the film thickness remained rather large. Solutal Marangoni flow was considered in [235]; the dependence of the saturated vapor density on the concentration of the dissolved substance in solution was taken into account in [234]. These works numerically investigated the modes of deposition depending on the speed of the substrate and studied periodic deposit structures for several parameter values [234, 235]. Practically the same problem statement was studied in [236, 237], which also used the hydrodynamic model, but the role of the wetting and periodic pinning/depinning effects of the moving contact line in the formation of various lines from deposits was also investigated. The authors analyzed the dependence of sediment properties on numerous experiment parameters.

A simplified model of the evaporation of a droplet of a polymer solution with the compensatory flow, diffusion of the dissolved substance, and the separation of liquid and gel parts of the droplet taken into account was proposed in [238]. It used the lubrication approximation, while the droplet surface was found quasistatically and was approximated by a parabolic curve with

time-dependent factors. The vapor flux density was assumed to be constant in the area of the solution and equal to zero in the area of the gel part. The model allows distinguishing between final deposits of the basin, crater, and mound types depending on the problem parameters. The influence of the surface gel film on the evaporation rate of the solvent and on the collective diffusion coefficient was studied in [239] for polymer solutions drying on a solid substrate.

There are other models that could be applied to problems of evaporative lithography with some modifications [66]. We next consider approaches to modeling processes of evaporation lithography developed to date.

### 3.2. Modeling of evaporative lithography processes

Several models have been developed for evaporative lithography. These models are based on different approaches, for example, the kinematic approach or the lubrication approximation. Different methods are used to solve these problems, for example, the finite-difference method (FDM) or the finite element method (FEM). As a rule, processes are considered in liquids (single-phase models without film solidification). Two-phase models are used less frequently because they are complex. In reality, different phase transitions occur as the volatile substance is lost, for example, a liquid–vapor phase transition, glass formation during melting and cooling of a polymer sediment, a sol–gel transition, and salt crystal formation as the solution concentration increases. Some models take multiphase systems into account. Certain flow types dominate in different complex systems, for example, Marangoni or Rayleigh–Bénard convection, capillary flow, etc. Additional effects including sedimentation, coagulation, etc., must often be considered.

We consider the most used approaches to mathematical modeling of different processes in evaporative lithography and the corresponding approximations. We classify the methods that do not use the fluid motion equations obtained from the momentum conservation law under the kinematic approach. In such studies, the flow velocity is expressed based on the mass conservation law, while the motion and shape of the two-phase liquid–air interface are defined based on various assumptions using an approximation. The term “kinematic approach” was selected because such models do not consider the causes of the flow (forces, pressure gradients, etc.), nor do they explicitly include such parameters as fluid viscosity, for instance. The equilibrium free surface of thin droplets is often approximated at each instant using the parabolic approximation where the parameters of the parabola depend on the time and the evaporation rate. A flat free surface is sometimes used for films, with the film height linearly decreasing over time proportionally to the evaporation rate. Local free surface curvatures and the deviation from the equilibrium shape are possible in real systems. They can be caused both by internal and external forces. Such curvatures can often be almost imperceptible, but it is precisely these curvatures that cause capillary flows in microdroplets or flows caused by the hydrostatic pressure gradient in macrodroplets. The kinematic models do not explain this phenomenon.

Models can be classified into continuous and semidiscrete [240]. In semidiscrete models, the fluid flow is described



continuously using the mass and momentum conservation laws, while the dynamics of each individual particle is considered. In the continuous approach, particle redistribution is described based on the convection–diffusion equation [238, 232] in terms of concentration. The discrete approach that explicitly describes individual particles and liquid molecules is computationally intensive and hence rarely used [240]. In the semidiscrete approach, the particle dynamics are often simulated using dissipative particle dynamics [241] or the Monte Carlo method [242, 231]. The continuous approach is based on the Navier–Stokes equations

$$\rho \left( \frac{\partial \mathbf{v}}{\partial t} + (\mathbf{v} \cdot \nabla) \mathbf{v} \right) = -\nabla P + \mu \Delta \mathbf{v} \quad (1)$$

and the continuity equation

$$\nabla \cdot \mathbf{v} = 0. \quad (2)$$

Here,  $\rho$  is the liquid density,  $\mu$  is the viscosity,  $P$  is the pressure, and  $\mathbf{v} = (\mathbf{u}, w)$  is the flow velocity vector, where  $\mathbf{u}$  is the velocity vector in a plane section parallel to the substrate and  $w$  is the velocity component perpendicular to the substrate. We note that gravity is disregarded in (1). This applies when the typical size of the liquid is less than the capillary length. In an axisymmetric case, it is often convenient to write Eqs. (1) and (2) in terms of the stream function and vorticity, thus eliminating the unknown function  $P$  [31].

If the fluid layer is relatively thin, then using the lubrication approximation is often acceptable [243, 244]. System of equations (1), (2) is then simplified and becomes

$$\mu \frac{\partial^2 \mathbf{u}}{\partial z^2} - \tilde{\nabla} P = 0, \quad -\frac{\partial P}{\partial z} = 0, \quad \tilde{\nabla} \mathbf{u} + \frac{\partial w}{\partial z} = 0, \quad (3)$$

where  $\tilde{\nabla}$  is the horizontal projection of the gradient. The formulation of the boundary conditions varies in different studies and depends on the particular problem. If two expressions with pressure from (3) are integrated with the particular boundary conditions taken into account, then explicit equations for  $\mathbf{u}$  and  $w$  can be obtained [244]. The flow velocity averaged over the fluid layer thickness is

$$\bar{\mathbf{u}} = \frac{1}{h} \int_0^h \mathbf{u} dz.$$

The value of  $z = h$  corresponds to the position of the liquid–air interface.

It is often appropriate to use the lubrication approximation together with the kinematic approach. Analytic expressions for the fluid flow velocity that are applicable for a sufficiently small film height or sufficiently small droplet contact angle can then be obtained. In [245, 30], analytic velocity expressions were obtained for a thin droplet, and the velocity field was compared with the results of numerical simulation. The compensatory flow was studied in [245], and Marangoni flow was studied in [30]. If the droplet surface is approximated by a spherical cap

instead of a parabola, then analytic expressions can be obtained for the lubrication approximation, which are applicable with good accuracy for a significantly broader range of contact angles, while the expression complexity barely increases [246]. If the kinematic approach is used, even more accurate but cumbersome analytic approximations for the velocity field can be obtained without using the lubrication approximation at all [246]. We next discuss works related to the mathematical modeling of processes in evaporative lithography.

The model in [142] describes the mass transfer of a nonuniformly dried aqueous latex film. A lubrication approximation was used in [142] to derive the basic equations of the model. The evaporation rate was assumed to be constant in the open areas, and no evaporation was assumed in the masked areas. Compensatory flows appear as a result of deformation of the free surface and evaporation. In the vertical direction, the Peclet number is equal to zero, and it is hence believed that the particles are evenly distributed throughout the thickness of the thin film. In the horizontal direction, the Peclet number is equal to infinity, and particle diffusion is hence not taken into account. Using the mass conservation law, the authors obtained the equation for the time-dependent film thickness

$$\frac{\partial h}{\partial t} + \tilde{\nabla} (h \bar{\mathbf{u}}) = -\frac{Jl}{\rho}, \quad (4)$$

where the vapor flux density  $\tilde{J}$  is equal to 0 or  $J_0$  depending on the spatial coordinate ( $J_0 > 0$  is a constant). It mimics the effect of the mask on evaporation. The notation  $l = \sqrt{1 + (\tilde{\nabla} h)^2}$  is used in (4). In [142],  $l = 1$  for the flat free surface of the liquid and also the flow rate  $\bar{u} = \sigma / (3\mu) h^2 \partial^3 h / \partial x^3$  obtained from (3) were used in the case of the single horizontal direction  $x$  by considering a boundary condition for  $P$  at the surface using the capillary pressure ( $\sigma$  is surface tension). The particle transfer equation was formulated in terms of the mass fraction  $\phi$ ,

$$\frac{\partial (h\phi)}{\partial t} + \tilde{\nabla} (\phi h \bar{\mathbf{u}}) = 0. \quad (5)$$

Along with the capillary flow in the liquid film, the fluid filtration in the solid film, where the mass fraction of particles reaches a critical value  $\phi_m = 0.64$  corresponding to the random dense packing of spheres, was taken into account in [142]. Darcy’s law was only used to derive the motion of the liquid front of the film, which moves as the solid part dries completely. An additional equation that allows explicitly defining the film front with dense packing of particles was also obtained in [142]. The problem was solved numerically using the fourth-order Runge–Kutta method. The authors reported a natural experiment in [142] (Fig. 3). Its results agreed qualitatively with the results of their numerical solution. In the final film profile, there were dips in the area where the evaporation was blocked by the mask. This is due to an outflow of mass from such an area to the areas where evaporation occurs. The capillary flow compensates for the loss of vaporized mass.

As previously mentioned (see Sec. 2.1), Deegan et al. [27] considered three modes of evaporation in their experiments. They applied their mathematical model to only one of these

modes, where the evaporation rate increases towards the three-phase boundary. The given explanation of the coffee-ring effect was based on a simple kinematic model [27]. In this model, the dissolved substance is carried to the contact line by compensatory fluid flow. The droplet profile  $h$  was approximated by a spherical cap shape. This droplet geometry is typical of small liquid volumes where capillary forces dominate the gravitational forces. Experimental measurements [27] confirm that the approximation of  $h$  by the equilibrium form is allowable. The height-averaged radial velocity of the compensatory flow caused by evaporation in [27] was expressed from the mass conservation law (4),

$$\bar{u}(r, t) = -\frac{1}{\rho r h} \int_0^r dr r \left( J(r, t) \sqrt{1 + \left( \frac{\partial h}{\partial r} \right)^2} + \rho \frac{\partial h}{\partial t} \right).$$

Particle transfer equation (5) written in cylindrical coordinates was also included in the model [27]. The diffusion-limited evaporation model was used to calculate the vapor flux density  $J$ . If evaporation can be regarded as an adiabatic process in the sense that the vapor concentration adjusts sufficiently rapidly to a change in the drop size and shape, then the Laplace equation with the corresponding boundary conditions can be used as an approximation to the diffusion equation for vapor in air. An analytic approximation based on the exact solution of the Laplace equation obtained in toroidal coordinates was proposed. The problem was shown to be mathematically equivalent to the known problem of the electrostatic potential of a charged conductor with a shape defined by two intersecting spheres. The disadvantage of the approximation  $J \approx J_0 f(\lambda) [1 - (r/R)^2]^{-\lambda}$  proposed in [27] is that  $J \rightarrow \infty$  at the three-phase boundary. Here,  $R$  is the contact line radius, and  $\lambda$  and  $f$  can depend on  $\theta$  [27]. An alternative mechanism for the coffee-ring effect was proposed in [247], where the authors showed numerically that the fluid flow in an evaporating droplet can entrain the particles to the liquid–gas interface, where the particles can be captured by the surface. The particles are further carried on along the interface until they reach the contact line.

Another model based on the lubrication approximation was used for a thin axisymmetric droplet of diluted colloidal solution [244]. As in [142, 27], thermal processes were not taken into account. Mass transfer in liquids was considered at the initial stage long before the gel phase formation (single-phase model). The droplet shape was determined by an equation derived from the mass conservation law for the solution (4). For a thin drop, a simple case of  $l \approx 1$  was considered. The dynamics of mass fraction of particles in space and time were described by the transfer equation. The flow velocity field and radial velocity averaged over the liquid layer thickness were derived from (3) taking into account capillary pressure in the absence of Marangoni flow. The purpose was to describe the process mathematically for three different evaporation modes corresponding to the experiments [27] (Fig. 2). The case where the vapor flux density dominates near the periphery was de-

scribed by the model law

$$J = \frac{J_0}{K + h(r, t)/h_0} \left( 1 - e^{-A(r-R)^2/R^2} \right),$$

where the parameter  $A$  sets the decrease rate of  $J$  near the three-phase boundary and the nonequilibrium parameter  $K$  determines the difference between the evaporation rate in the droplet center and near the periphery ( $K \rightarrow 0$  in the case of a rapidly evaporating liquid and  $K \rightarrow \infty$  for a nonvolatile liquid). Here,  $J_0 \approx k \Delta T / (L h_0)$  is the vapor flux density at the droplet apex, where  $k$  is the thermal conductivity of the liquid,  $L$  is the latent heat of vaporization,  $h_0 = h(0, 0)$  is the initial droplet height, and  $\Delta T$  is the difference between the saturation temperature and the substrate temperature. The case where evaporation is uniform was described by the model law

$$J = \frac{J_0}{4h(0, t)/h_0} (1 - \tanh[A(r - r_0)/R]),$$

where the parameter  $r_0$  defines the point near the three-phase boundary where  $J$  tends to zero. The third case, where evaporation prevails at the symmetry axis, was described by the model law

$$J = \frac{2J_0}{h(0, t)/h_0} e^{-Ar^2/R^2}.$$

The three model evaporation laws in [244] are approximations derived from different considerations describing the process at a qualitative level. These approximations take into account that the pinning occurs due to the accumulation of particles near the three-phase boundary [248]. Therefore, in these model laws,  $J \rightarrow 0$  as  $r \rightarrow R$ . In reality, the vapor flux density strongly depends on the particle concentration in the solution [249, 250, 251]. This is especially true for concentrated solutions. Further, the numerically implicit Gear method was applied to the problem at different values of the main parameters (evaporation number and capillary number). The velocity field, the dynamics of the particle distribution, the evolution of the droplet surface shape, the change in liquid volume, and the contact angle dynamics during evaporation were obtained in [244].

The effect of external laser beam heating on the transport of nanoparticles and liquid in a sessile droplet on a flat horizontal substrate was studied numerically in [252]. Parameters such as the laser radiation intensity, beam diameter, solution absorption factor, and thermal conductivity of the substrate were studied. The model takes the thermocapillary flow and droplet shape change under the influence of laser radiation into account. In the absence of radiation, the model demonstrated the droplet shape as a spherical segment, which is typical of a size that is smaller than the capillary length. When exposed to the laser, the shape of the droplet was curved, and a dimple appeared in the center. An increase in temperature in local areas leads to a reduction in surface tension. When the diameter of the beam is comparable to the size of the droplet base, the surface shape becomes unstable, and ripples appear in the form of waves. The model in [252] is based on the Navier–Stokes equations written in Lagrangian coordinates. In addition, the possible coagulation of particles was also taken into account. The Galerkin finite

element method was used in [252] to solve the problem. Unfortunately, this model does not describe the final structure of the deposit after the exposure to laser radiation and the complete evaporation of the droplet.

A method based on the effect of periodic air flow on the evaporation of a polymer solution film was proposed in [253]. A liquid with polymer particles is applied to a substrate above which there is an array of airflow sources (Fig. 22). The system has several geometric parameters: the nozzle hole width  $B$ , the distance  $2W$  between adjacent nozzles, and the distance  $H$  between the initial position of the two-phase boundary and a nozzle. The substrate moves at a certain speed  $U$ , which is also one of the system parameters. This method was studied numerically [253]. The mathematical model is based on the lubrication approximation, and the expression for velocity takes not only the capillary flow but also the Marangoni flow into account,

$$\bar{u} = -\frac{h^2}{3\mu} \frac{\partial P}{\partial x} + \frac{h}{2\mu} \frac{d\sigma}{dx}.$$

Here, the Laplace pressure is  $P = -\sigma \partial^2 h / \partial x^2$ . In the model [253], the viscosity  $\mu$  and surface tension  $\sigma$  are expressed through empirical dependences on the temperature and particle concentration. The vapor flow density is described by a semiempirical dependence that takes the difference in vapor pressure near and away from the free film surface into account. The substrate motion is simulated by changing the Biot number and Nusselt number over time. In [253], an implicit finite-difference scheme on an irregular mesh was used to solve this problem. The discretized scheme was solved by the Thomas algorithm. Numerical calculations showed that a moving coating (polymer solution) is subject to asymmetric changes in thickness, which increases and levels sequentially.

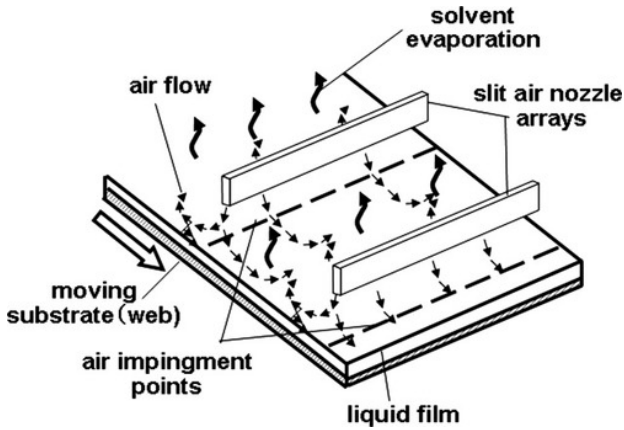


Figure 22: Coated film on a moving substrate is periodically blown by air from slit nozzles. Reprinted with permission from Ref. [253]. Copyright 2009 American Institute of Chemical Engineers (AIChE).

The effect of external laser heating on the formation of the relief coating was simulated in [181]. A two-dimensional area was considered, which can be divided into several subareas: the substrate, the liquid heatsink under the substrate, the film on the substrate, and the air area above the film. The problem

was solved in several stages. (1) The temperature distribution due to IR illumination was calculated. (2) The solvent vapor transport was calculated, and the vapor flux density was determined. (3) The distribution of the dissolved substance in the liquid layer was simulated. The first stage involved solving the equation

$$\rho(x, y) c(x, y) \mathbf{v} \cdot \nabla T = \nabla \cdot [k(x, y) \nabla T + q_v],$$

where  $T$  is the temperature,  $k$  is the liquid heat conductivity, and  $c$  is the specific heat capacity. The cooling flow velocity  $\mathbf{v} = [u(y), 0]$  in the heatsink was determined explicitly ( $\mathbf{v} = 0$  in the substrate and the film). The volume heat flux density is  $q_v = a I(y) H(x)$ , where  $a$  is the absorption coefficient,  $I$  is the radiation intensity, and  $H$  is the Heaviside function for modeling of selective heating of a certain area. In the second stage, after a stationary temperature profile on the film surface is found, the convective and diffusion transfer of solvent vapor in the air area above the film was simulated. This stage is described by three equations: the equation of motion for the airflow velocity  $\mathbf{v}$  and the convection–diffusion equations for air temperature  $T$  and for the vapor concentration  $s$ . The vapor flux density at the two-phase boundary is defined as  $J(x) = D_v \mathbf{n} \cdot \nabla s$ , where  $\mathbf{n}$  is the normal vector to the free surface and  $D_v$  is the vapor diffusion coefficient. In the third stage, the mass transfer of the substance in the liquid was calculated. Different approaches were used for relatively thin and thick liquid layers. In the first case, the model includes a one-dimensional particle mass fraction convection–diffusion equation averaged over the liquid layer thickness and the free surface dynamics equation based on the mass conservation law. The height-averaged radial velocity is found using the lubrication approximation. The hydrostatic and capillary pressure and also the dependence of the surface tension on the concentration and temperature are taken into account. In the second case, the model includes a two-dimensional convection–diffusion equation and the equation of motion. The arbitrary Lagrangian–Eulerian (ALE) scheme was used in [181] to describe the deformation of the liquid–air interface. The results of the numerical calculations in [181] showed the dynamics of film thickness and particle concentration in space and time. The dependence of the final structure on the width of the laser beam was also shown.

The evaporation of a colloidal film under a solvent-permeable membrane with periodic thicknesses was studied theoretically in [254]. The essence of the proposed method is that evaporation occurs more rapidly in those subregions where the thickness of the membrane is thinner (Fig. 23).

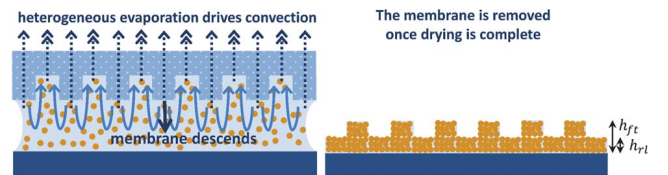


Figure 23: Schematic representation of a film evaporation method under a topographically patterned membrane. Reproduced from Ref. [254] with permission from The Royal Society of Chemistry.



Mass transfer was numerically calculated in the proposed system [254]. The model includes convection–diffusion and Navier–Stokes equations. An incompressible liquid is assumed, and the continuity equation is hence stationary. The driving factor in the system is the osmotic pressure gradient, which is part of the equation of motion. The vapor flux density is defined using the formula  $J = \bar{p}\Delta P/d$ , where  $\bar{p}$  is the membrane permeability factor,  $\Delta P$  is the partial pressure driving force, and  $d$  is the membrane thickness. The calculation results showed that the concentration of particles in the area where the thickness of the membrane is smaller increases. As a result, a solid film of periodic thickness is obtained. The key parameters for regulating the final pattern are the geometric characteristics of the membrane along with the initial film thickness and the solution concentration.

The evaporation of an aqueous latex film under a mask and an IR lamp (see Sec. 2) [161] was simulated in [255]. The model includes a convection–diffusion equation with a source term,

$$\frac{\partial C}{\partial t} + \bar{u} \frac{\partial C}{\partial x} = \frac{D_s}{h} \frac{\partial}{\partial x} \left( h \frac{\partial C}{\partial x} \right) + \frac{JCl}{\rho h}, \quad (6)$$

mass conservation law (4), the heat transfer equation for the liquid

$$\begin{aligned} \frac{\partial T}{\partial t} + \bar{u} \frac{\partial T}{\partial x} = & \frac{1}{c\rho h} \frac{\partial}{\partial x} \left( kh \frac{\partial T}{\partial x} \right) - \frac{Jl}{\rho h} \left( \frac{L}{c} - T \right) + \\ & + \alpha \frac{T_s - T}{c\rho h} + q \frac{1 - \exp(-ah)}{c\rho h} H(X_h - x), \end{aligned} \quad (7)$$

and the heat conduction equation for the substrate

$$\begin{aligned} \frac{\partial T_s}{\partial t} = & \frac{1}{c_s \rho_s} \frac{\partial}{\partial x} \left( k_s \frac{\partial T_s}{\partial x} \right) + \alpha \frac{T - T_s}{c_s \rho_s h_s} + \\ & + q \frac{\exp(-ah)}{c_s \rho_s h_s} H(X_h - x). \end{aligned} \quad (8)$$

Here,  $D_s$  is the diffusion coefficient,  $2X_h$  is the mask hole width,  $\alpha$  is the convective heat transfer coefficient,  $L$  is the latent heat of evaporation, and  $q$  is the surface density of the radiation power. The particle mass fraction  $C$  and the temperature  $T$  are height-averaged functions. In (8), the subscript  $s$  denotes the substrate. The local impact of the emitter is described using the Heaviside function  $H$ . The model [255] accounts for such effects as diffusive and convective particle transport, thermodiffusion of heat in the liquid and substrate, convective heat transfer in the liquid, film cooling by evaporation, liquid and substrate heating by IR light, and heat transfer between the liquid and substrate. Equations (6), (7), and (8) are derived from the conservation laws when considering mass and heat balance in an elementary volume. The capillary flow rate  $\bar{u} = \sigma/(3\mu)h^2 \partial^3 h/\partial x^3$  is determined with the lubrication approximation in [255] ( $l = 1$  in this case). An empirical formula is used to describe the dependence of the viscosity  $\mu$  on the particle concentration. In [255], the liquid–solid phase transition is assumed to occur when a critical solution concentration  $C_g = 0.7$  is reached. A theoretical formula taking the dependence of the evaporation rate on the liquid temperature

into account is used for the vapor flux density. This formula was modified to also take the effects of particle concentration and the mask hole size into account. As a result of numerical calculations, the dynamics of the temperature, the particle mass fraction, the liquid–glass boundary, the vapor flux density, and the free surface of the film were obtained [255]. The final thickness of the solid patterned film agrees well with the experiment [161]. At the end of the process, the value of  $h$  varies between 3 and 80  $\mu\text{m}$ . The capillary flow velocity initially increases because the vapor flux density increases. Subsequently, it begins to decrease as the viscosity increases.

A method for obtaining concentric deposits of colloidal particles was proposed in [256] (Fig. 24). A mask geometry with annular holes was used. The method was studied theoretically and computer simulations were performed.

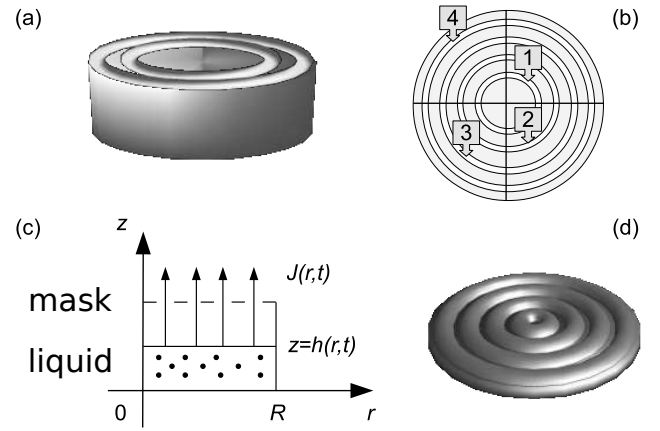


Figure 24: (a) Cylindrical cell covered with a mask on top. (b) A mask with four annular holes. (c) Problem domain. (d) The expected result for particle redistribution and formation of a solid phase in the form of concentric rings [256].

The non-steady-state model [256] is based on one-dimensional equations obtained based on mass and momentum conservation laws. The model includes the convection–diffusion equation, the film thickness evolution equation, and the equation of motion for a viscous fluid, all written in cylindrical coordinates. The process is described in the initial stage when the solution can be regarded as dilute. In [256], the capillary flow is taken into account, which is typical of a microcell smaller than the capillary length. A subsequent modification of the model [257] also takes the hydrostatic pressure into account (additional term in the equation of motion), which allows considering the process in a macrocell. We note that the model in [257] does not use the lubrication approximation; the flow velocity is obtained from the 1D equation of motion and  $l \neq 1$  in (4), in (6), and in the expression for the capillary pressure obtained by considering the Young–Laplace equation and the curvature of an axisymmetric surface,

$$P = -\sigma \left( \frac{1}{\bar{p}} \frac{\partial^2 h}{\partial r^2} + \frac{1}{rl} \frac{\partial h}{\partial r} \right).$$

This model thus accounts for the curvature of the two-phase boundary, which is not always flat. The shape of the free surface of the liquid in the microcell differs from that of the macrocell

because of competition between the capillary and gravitational forces. The approximation  $J = J_0[1 - \cos(2\pi rN/R)]/2$  is used for the vapor flux density, which agrees qualitatively with the numerical calculations [143]. Here,  $N$  is the number of circular holes in the mask, and  $R$  is the cell radius. The results of the calculations show that the flow carries particles into the areas under the mask holes. Over time, the mass fraction of particles in these areas increases. As the evaporation rate increases, the difference in solution concentration in closed and open areas also increases. With slow evaporation, the difference is smoothed. The reason for this is the competition between diffusion and convection transfer.

The experiment in [143] with evaporation of a colloidal liquid under a mask was simulated in [258, 259]. The two-dimensional model is based on the mass conservation law for a suspended substance and a liquid. The motion of the liquid–air boundary is set by explicitly assuming that it is always flat. The equilibrium free boundary is calculated based on an estimate of the evaporation rate. The height-averaged radial flow velocity  $\bar{u}(x, y)$  is determined from the mass conservation law. A compensatory flow caused by evaporation is considered. The convection–diffusion equation contains an additional term to account for particle deposition (particle adhesion to the substrate). The vapor flux density in [258] is described by the model law  $J(r, \varphi) = J_0 \sin^2(\pi r/R) \sin^2(m\varphi/2)$ , where the constant  $m$  corresponds to the number of symmetrically located holes in the mask above the drop. The local vapor flux density  $J$  at the two-phase boundary in [259] is determined using the solution of the Laplace equation for the vapor concentration in the air area. The value of  $J$  was calculated for the initial film height. The dependence of this solution on the further dynamics of the free surface was not considered. The effect on the mass transfer of parameters such as the distance between the mask and liquid, the ratio of the mask hole radius to the hole distance, the particle deposition rate, the diffusion coefficient value, and the initial particle fraction was considered in [259].

The appearance of asymmetric precipitation during the evaporation of two adjacent droplets was studied in [260]. A similar experiment was performed previously, for example, in [27]. The simple model of a thin drop proposed in [260] describes a process in a two-dimensional region parallel to the substrate. The shape of the drop is determined by a parabolic approximation. The height-averaged radial velocity is found from the solution mass conservation law (4). The time dependence of the droplet base radius is determined based on the Onsager variational principle. A linear approximation is used for the nonuniform vapor flux density. The initial particle positions are randomly generated from a uniform distribution. Only the lateral flow transfer is taken into account. Depending on the parameters controlling the evaporation and friction of the contact line, the model [260] predicts fan-like and eclipse-like deposition patterns.

A mathematical model was developed in [182] for the active method of evaporative lithography where a source of dry airflow in the form of a concentric nozzle is located above the film (see Sec. 2). The problem was solved in two domains, namely, in a liquid film and in the air above it. Steady-state

equations were used for the air domain. The model in [182] describes the airflow velocity using the equation of motion. The vapor concentration is described by the convection–diffusion equation. Solving these equations allows calculating the vapor flux density on the free surface of the film. In addition, when calculating  $J$ , the authors [182] roughly considered its dependence on the particle concentration at the two-phase boundary. The nonsteady equations were used to describe mass transfer in the film. In the equation of motion, viscosity was taken out of the derivative, but in this case, its dependence on the particle concentration was described (and depends implicitly on space coordinate). The particle transfer was described by the convection–diffusion equation, where the diffusion coefficient is assumed to be constant. The ALE method was used in [182] to solve the problem. The dynamics of film thickness and particle concentration in space and time were described using numerical simulations. The final thickness of the solid film for different values of dry air flow rate from the concentric nozzle was obtained. The numerical results agreed qualitatively (in some cases quantitatively) with the experimental results [182].

In [194], a 1D model based on the lubrication approximation was used to justify the experimental method mathematically (see Sec. 2.3). The expression for the height-averaged flow velocity takes the effect of capillary pressure, solutal Marangoni flow, and substrate motion into account. The viscosity depends on the concentration of the solution and is described empirically. The evaporation rate depends linearly on the concentration of the polymer solution in the model [194].

As a part of the analysis of the state-of-the-art in this direction, Table 2 contains comparative characteristics of the models. Further developments in modeling of the formation of micro- and nanostructures with nonuniform evaporation of droplets and films will allow a better understanding the basic mechanisms, finding out how to manage the process, and obtaining particle deposit forms with greater spatial accuracy.

#### 4. Conclusions and outlooks

Evaporative lithography is a new, actively developing field. This type of lithography is based on generating ambient conditions for nonuniform evaporation along the free surface of a droplet or film. The resulting convection flows can be caused by different forces, but their initial cause in any case is evaporation. For example, compensatory flows caused by the deviation of the free surface shape from the equilibrium position can be induced by both capillary and gravitational forces. Nonuniform evaporation often results in a variation of fluid temperature and solution concentration on the free surface. This results in a surface tension gradient, causing Marangoni flows to emerge. If temperature and concentration gradients occur in the bulk, then Rayleigh–Bénard flows arise associated with the heterogeneity of density. Other mechanisms of flow generation are also possible that eventually carry the dissolved substance or particles suspended in liquids to the required local areas, forming spatially patterned deposits in a controlled manner.

Evaporative lithography methods can be divided into active and passive. In passive methods, the key parameter values are

Table 2: Comparative characteristic of models

Models vs. characteristics	Viscosity	Diffusion	Flow type	Vapor flux density	Solidification in a liquid	Heat transfer	Other effects	Approaches and methods	Comparison with experiments	Dimension
Roth & Russel, 1998 [142]	constant	–	Capillary flow. Darcy's law is partially taken into account.	Constant value. No flux in the masked area.	The liquid-solid interface is tracked explicitly in a film.	–	–	Lubrication approximation. Fourth-order Runge-Kutta method.	Qualitative comparison with [142].	1D
Degan et al., 2000 [27]	Not taken into account explicitly, because there is no equation of motion.	–	Compensatory flow from the mass conservation law.	Analytic approximation based on the solution of the Laplace equation for vapor taking the electrostatic analogy into account.	Single-phase model.	–	–	Kinematic approach with an equilibrium droplet shape in which the flow velocity is determined from the conservation mass law. Analytic solution.	Qualitative comparison with [27].	1D
Fischer, 2002 [244]	constant	–	Capillary flow.	Three model evaporation laws simulating the experiment [27].	Single-phase model.	–	–	Lubrication approximation. Implicit Gear method.	Qualitative comparison with [27].	1D
Dietzel & Poulisakos, 2005 [252]	constant	Depends on particle concentration and temperature.	Thermocapillary flow.	Energy and mass balance analysis for the heated spherical droplets, taking the diffusion of vapor in air and the Stefan flow into account.	Single-phase model.	Thermal diffusion in liquid and substrate. Laser heating of a free surface part.	Coagulation of particles.	Navier-Stokes equations, written in Lagrange coordinates. FEM.	–	2D
Yamamoto et al., 2009 [253]	Depends on particle concentration and temperature.	Depends on particle concentration.	Capillary flow. Marangoni convection. Surface tension depends on temperature and particle concentration.	A semi-empirical formula based on the difference in vapor pressure near the free surface of the film and away from it.	Single-phase model.	Change in liquid and substrate temperature. Evaporative cooling. Heat transfer from the air.	Simulation of a moving substrate under periodically arranged nozzles.	Lubrication approximation. Implicit difference scheme on a nonuniform mesh. The discretized scheme was solved by the Thomas algorithm.	–	1D
Vieyra Salas et al., 2012 [181]	Depends on the solute concentration.	Depends on the solute concentration.	Flow caused by capillary and hydrostatic pressure gradients. Marangoni convection caused by the concentration and temperature gradients on the free surface.	Convection-diffusion equation for the vapor is solved.	The two-phase boundary is tracked implicitly.	Laser film heating. Cooling due to evaporation, adhesion, and heat transfer to the air. Heat transfer in air and liquid heatsink. Substrate cooling with the heatsink. Thermal diffusion in a liquid and substrate.	–	The steady-state heat transfer equation for the liquid in the heatsink and thermal conductivities of the substrate and the film. Hydro- and aerodynamic equations. ALE method.	Qualitative comparison with [181].	2D
Arshad & Bomezuze, 2013 [254]	Depends on particle concentration.	Depends on particle concentration.	Flow caused by osmotic pressure gradient.	Depends on the thickness of the membrane.	The two-phase interface is tracked implicitly.	–	–	Navier-Stokes equations, convection-diffusion FEM.	–	2D
Vodolazkaya & Tsvetkov, 2017 [259]	–	constant	Compensatory flow from the mass conservation law.	Solving the vapor diffusion equation in ambient air for the initial film height.	Single-phase model.	–	Adhesion of particles to the substrate.	Equations based on the conservation mass law. Kinematic approach in flow velocity calculation. FEM.	Qualitative comparison with [43].	2D
Hu et al., 2017 [260]	–	–	Compensatory flow from the mass conservation law.	Linear approximation.	Precipitation over the contact line.	–	Contact line movement.	Kinematic approach. Contact line dynamics is determined by the Onsager variational principle.	Qualitative comparison with [27, 166, 167].	2D
Kolagov & Lobanov, 2018 [257]	constant	const	Flow caused by the capillary and hydrostatic pressure gradient.	Depends on the spatial coordinate. Minimizes the mask influence.	Single-phase model.	–	–	The equation of motion, the solution has a diffusion law, the convection-diffusion equation. FDM.	–	1D
Widerblovskiy et al., 2018 [182]	Depends on particle concentration.	constant	Capillary flow.	Depends on the vapor and particle concentrations near the free surface.	The two-phase boundary is tracked implicitly.	–	–	Hydro- and aerodynamic equations. ALE method.	Qualitative comparison with [182].	2D
Widerblovskiy et al., 2018 [194]	Depends on particle concentration.	constant	Capillary & Marangoni flow	Depends on particle concentration.	The two-phase boundary is tracked implicitly.	–	Substrate motion.	Lubrication approximation. FEM.	Qualitative comparison with [194].	1D
Kolagov, 2018 [255]	Depends on the particle concentration.	constant	Capillary flow.	Depends on temperature, particle concentration, and coordinate (minimizes mask effect).	The two-phase boundary is tracked implicitly.	External lamp heating. Heat transfer in a liquid. Thermal conductivity in a substrate. Heat exchange between the liquid and substrate. Evaporative cooling.	–	Equations based on the mass and energy conservation laws. Flow velocity calculation via lubrication approximation. FDM.	Qualitative comparison with [161].	1D



set initially (the mask hole size, the liquid–mask gap width, the initial particle concentration or film thickness, the distance between the holes, the geometry of the membrane, etc.). In contrast to passive methods, active methods are characterized by the presence of key parameters that can be adjusted in real time (radiation power, airflow velocity, substrate motion speed, etc.). This allows dynamically influencing the geometry of the pattern being formed. Hybrid methods that combine evaporative lithography with other EISA or non-EISA approaches can be identified as a separate subgroup. This expands the possibilities of evaporative lithography, which stimulates active research in this area. The great interest in evaporative lithography is driven by many promising applications in various fields. Let us mention just a few of them. The creation of transparent flexible conductive films and organic transistors is extremely important for optical and microelectronics. In nanotechnologies, special attention is paid to functional coatings where the obtained thin-film pattern has the required physical and chemical properties. New miniature instruments are created for health care development allowing express-diagnostics and delivery of drugs to particular parts of the human body.

Along with experimental studies, mathematical models are being developed and improved. Theoretical and numerical studies facilitate understanding of the physical processes occurring in evaporative lithography. Modeling allows identifying key system parameters and facilitates the determination of the range of parameter values for efficient control over patterns formation with the required geometric and physicochemical characteristics. Currently, there are several models describing the process of heat and mass transfer in evaporative lithography. In most cases, these are one-dimensional and/or single-phase models that take only individual processes at a qualitative level into account. Development in this direction is relatively slow because the phenomena and processes observed in evaporative lithography are complex.

As a rule, the height of formed sediments and hard coverings varies from one micron [163, 173, 178] to several tens [142, 143, 161] or hundreds of microns [223]. In a plane parallel to the substrate surface, the size of individual structure elements ranges from hundreds of microns [215, 223, 177] to several millimeters [142, 219, 175, 162]. In this respect, evaporative lithography is inferior to some other EISA methods, which allow obtaining stripes of 10 microns or less in width [93, 95]. Further development of evaporative lithography will allow obtaining patterned deposits and solid patterned films with more accurate spatial resolution. This will allow forming non-blurred patterns on the substrate. Such micro- and nanostructures may be further needed for new applications in the biosensors, labs-on-chip, functional coatings, and many others. For this, the existing passive and active methods must be improved. New methods must be also developed. A hybrid approach is most likely to achieve significant results.

It is hoped that further experimental studies of evaporative lithography will help resolve some of the existing technical difficulties. For example, one problem that deserves attention is the need to increase an area of a formed coating. This area is usually now measured in square millimeters or centimeters,

but such dimensions are insufficient for some applications. An example is the problem of microstructuring the surface a boat hull to obtain a coating that prevents the growth of marine organisms [261]. Further development of theoretical studies and mathematical modeling of evaporative lithography seems especially important in terms of improving the control over the pattern forming process. We believe that the development of more complete and hence more complex mathematical models requires a special focus. This primarily relates to multiphase and multidimensional simulations. Matters of interest include liquid rheology, flows in porous media, drop or film solidification (its phase transition into glass, gel, melt, etc.), thermal, physical, and chemical properties of the substrate (e.g., composite surfaces or porous wafers), and binary particle systems (including those with versatile shapes and properties).

## 5. Acknowledgment

This work is supported by the grant 18-71-10061 from the Russian Science Foundation.

## References

- [1] J. C. Maxwell, *Diffusion: collected scientific papers*, Encyclopedia Britannica, Cambridge, 1877.
- [2] I. Langmuir, The evaporation of small spheres, *Physical Review* 12 (1918) 368–370. doi:10.1103/PhysRev.12.368.
- [3] N. A. Fuchs, *Evaporation and droplet growth in gaseous media*, Pergamon Press, Oxford, 1959. doi:10.1016/C2013-0-08145-5.
- [4] M. Al Qubeissi, N. Al-Esawi, S. S. Sazhin, M. Ghaleeh, Ethanol/gasoline droplet heating and evaporation: Effects of fuel blends and ambient conditions, *Energy Fuels* 32 (6) (2018) 6498–6506. doi:10.1021/acs.energyfuels.8b00366.
- [5] P. Hänichen, A. Bender, B. Voß, T. Gambaryan-Roisman, P. Stephan, Drop evaporation of hydrocarbon fluids with deposit formation, *Int. J. Heat Mass Transfer* 128 (2019) 115–124. doi:10.1016/j.ijheatmasstransfer.2018.08.102.
- [6] J. E. Sprittles, Y. D. Shikhmurzaev, The dynamics of liquid drops and their interaction with solids of varying wettabilities, *Phys. Fluids* 24 (8) (2012) 082001. doi:10.1063/1.4739933.
- [7] V. Dugas, J. Broutin, E. Souteyrand, Droplet evaporation study applied to dna chip manufacturing, *Langmuir* 21 (20) (2005) 9130–9136, PMID: 16171342. doi:10.1021/la050764y.
- [8] S. Maheshwari, L. Zhang, Y. Zhu, H.-C. Chang, Coupling between precipitation and contact-line dynamics: Multiring stains and stick-slip motion, *Physical Review Letters* 100 (4). doi:10.1103/physrevlett.100.044503.
- [9] R. G. Larson, Transport and deposition patterns in drying sessile droplets, *AIChE J.* 60 (5) (2014) 1538–1571. doi:10.1002/aic.14338.
- [10] K. Sefiane, Patterns from drying drops, *Adv. Colloid Interface Sci.* 206 (2014) 372–381. doi:10.1016/j.cis.2013.05.002.
- [11] J. R. Trantum, D. W. Wright, F. R. Haselton, Biomarker-mediated disruption of coffee-ring formation as a low resource diagnostic indicator, *Langmuir* 28 (4) (2011) 2187–2193. doi:10.1021/la203903a.
- [12] Y. Masuda, T. Itoh, K. Koumoto, Self-assembly patterning of silica colloidal crystals, *Langmuir* 21 (10) (2005) 4478–4481. doi:10.1021/la050075m.
- [13] J. Wang, L. Wang, Y. Song, L. Jiang, Patterned photonic crystals fabricated by inkjet printing, *J. Mater. Chem. C* 1 (2013) 6048–6058. doi:10.1039/C3TC30728J.
- [14] Y. Zhao, L. Shang, Y. Cheng, Z. Gu, Spherical colloidal photonic crystals, *Accounts of Chemical Research* 47 (12) (2014) 3632–3642. doi:10.1021/ar500317s.

- [15] S. Fisenko, Y. Khodyko, O. Penyzkov, V. Saverchenko, Droplet evaporation on a substrate at the final stage of low pressure spray pyrolysis and the final morphology of nanoparticles, *International Journal of Heat and Mass Transfer* 78 (2014) 599–603. doi:10.1016/j.ijheatmasstransfer.2014.07.049.
- [16] V. Y. Gordeeva, A. V. Lyushnin, Dynamics of an evaporating thin film of polar liquid with solutocapillary marangoni effect and capillary osmosis, *Surf. Coat. Technol.* 320 (2017) 531–535. doi:10.1016/j.surfcoat.2016.11.025.
- [17] O. Kabov, Y. Lyulin, I. Marchuk, D. Zaitsev, Locally heated shear-driven liquid films in microchannels and minichannels, *International Journal of Heat and Fluid Flow* 28 (1) (2007) 103–112. doi:10.1016/j.ijheatfluidflow.2006.05.010.
- [18] E. Y. Gatapova, O. A. Kabov, Shear-driven flows of locally heated liquid films, *International Journal of Heat and Mass Transfer* 51 (19) (2008) 4797–4810. doi:10.1016/j.ijheatmasstransfer.2008.02.038.
- [19] O. Kabov, D. Zaitsev, V. Cheverda, A. Bar-Cohen, Evaporation and flow dynamics of thin, shear-driven liquid films in microgap channels, *Experimental Thermal and Fluid Science* 35 (5) (2011) 825–831. doi:10.1016/j.expthermflusci.2010.08.001.
- [20] F. Mahdi, T. Record, C. Amadi, F. Emmanuel, N. Ivanova, A. Trybala, V. Starov, Removal of submicron particles from solid surfaces using surfactants, *Colloids Interface Sci. Commun.* 6 (2015) 13–16. doi:10.1016/j.colcom.2015.10.001.
- [21] T. P. Bigioni, X.-M. Lin, T. T. Nguyen, E. I. Corwin, T. A. Witten, H. M. Jaeger, Kinetically driven self assembly of highly ordered nanoparticle monolayers, *Nature Materials* 5 (4) (2006) 265–270. doi:10.1038/nmat1611.
- [22] R. Picknett, R. Bexon, The evaporation of sessile or pendant drops in still air, *Journal of Colloid and Interface Science* 61 (2) (1977) 336–350. doi:10.1016/0021-9797(77)90396-4.
- [23] M. Shanahan, C. Bourges, Effects of evaporation on contact angles on polymer surfaces, *International journal of adhesion and adhesives* 14 (3) (1994) 201–205. doi:10.1016/0143-7496(94)90031-0.
- [24] C. Bourges-Monnier, M. E. R. Shanahan, Influence of evaporation on contact angle, *Langmuir* 11 (7) (1995) 2820–2829. doi:10.1021/la00007a076.
- [25] T. Kajiya, E. Nishitani, T. Yamaue, M. Doi, Piling-to-buckling transition in the drying process of polymer solution drop on substrate having a large contact angle, *Physical Review E* 73 (1) (2006) 011601. doi:10.1103/PhysRevE.73.011601.
- [26] R. D. Deegan, O. Bakajin, T. F. Dupont, G. Huber, S. R. Nagel, T. A. Witten, Capillary flow as the cause of ring stains from dried liquid drops, *Nature* 389 (6653) (1997) 827–829. doi:10.1038/39827.
- [27] R. D. Deegan, O. Bakajin, T. F. Dupont, G. Huber, S. R. Nagel, T. A. Witten, Contact line deposits in an evaporating drop, *Phys. Rev. E* 62 (1) (2000) 756–765. doi:10.1103/PhysRevE.62.756.
- [28] R. D. Deegan, Pattern formation in drying drops, *Phys. Rev. E* 61 (1) (2000) 475–485. doi:10.1103/PhysRevE.61.475.
- [29] D. Lohani, M. G. Basavaraj, D. K. Satapathy, S. Sarkar, Coupled effect of concentration, particle size and substrate morphology on the formation of coffee rings, *Colloids and Surfaces A: Physicochemical and Engineering Aspects* 589 (2020) 124387. doi:10.1016/j.colsurfa.2019.124387.
- [30] H. Hu, R. G. Larson, Analysis of the effects of marangoni stresses on the microflow in an evaporating sessile droplet, *Langmuir* 21 (9) (2005) 3972–3980. doi:10.1021/la0475270.
- [31] L. Y. Barash, T. P. Bigioni, V. M. Vinokur, L. N. Shchur, Evaporation and fluid dynamics of a sessile drop of capillary size, *Phys. Rev. E* 79 (2009) 046301. doi:10.1103/PhysRevE.79.046301.
- [32] H. Bénard, Les tourbillons cellulaires dans une nappe liquide propageant de la chaleur par convection: en régime permanent, *Rev. Gen. Sci. Pures Appl.* 11 (1900) 1261–1271.
- [33] J. R. A. Pearson, On convection cells induced by surface tension, *Journal of Fluid Mechanics* 4 (5) (1958) 489–500. doi:10.1017/S0022112058000616.
- [34] W. D. Ristenpart, P. G. Kim, C. Domingues, J. Wan, H. A. Stone, Influence of substrate conductivity on circulation reversal in evaporating drops, *Phys. Rev. Lett.* 99 (2007) 234502. doi:10.1103/PhysRevLett.99.234502.
- [35] L. Y. Barash, Dependence of fluid flows in an evaporating sessile droplet on the characteristics of the substrate, *International Journal of Heat and Mass Transfer* 84 (2015) 419–426. doi:10.1016/j.ijheatmasstransfer.2015.01.014.
- [36] J. M. Baek, C. Yi, J. Y. Rhee, Central spot formed in dried coffee-water-mixture droplets: Inverse coffee-ring effect, *Current Applied Physics* 18 (4) (2018) 477–483. doi:10.1016/j.cap.2018.01.007.
- [37] Y. Li, Q. Yang, M. Li, Y. Song, Rate-dependent interface capture beyond the coffee-ring effect, *Scientific Reports* 6 (2016) 24628. doi:10.1038/srep24628.
- [38] H. Kim, F. Boulogne, E. Um, I. Jacobi, E. Button, H. A. Stone, Controlled uniform coating from the interplay of marangoni flows and surface-adsorbed macromolecules, *Physical Review Letters* 116 (12) (2016) 124501. doi:10.1103/PhysRevLett.116.124501.
- [39] V. Ragoonanan, A. Aksan, Heterogeneity in desiccated solutions: Implications for biostabilization, *Biophysical Journal* 94 (6) (2008) 2212–2227. doi:10.1529/biophysj.107.110684.
- [40] T. Yakhno, Salt-induced protein phase transitions in drying drops, *Journal of Colloid and Interface Science* 318 (2) (2008) 225–230. doi:10.1016/j.jcis.2007.10.020.
- [41] K. Morinaga, M. Tani, R. Kurita, Formation mechanism of hierarchical structure of crystal morphology in a sessile droplet, *Physical Review Research* 2 (1). doi:10.1103/PhysRevResearch.2.013098.
- [42] D. Mampallil, H. B. Eral, A review on suppression and utilization of the coffee-ring effect, *Adv. Colloid Interface Sci.* 252 (2018) 38–54. doi:10.1016/j.cis.2017.12.008.
- [43] B. D. MacDonald, C. A. Ward, Onset of marangoni convection for evaporating sessile droplets, *Journal of colloid and interface science* 383 (1) (2012) 198–207. doi:10.1016/j.jcis.2012.06.046.
- [44] A. Marin, S. Karpitschka, D. Noguera-Marín, M. A. Cabrerizo-Vílchez, M. Rossi, C. J. Kähler, M. A. R. Valverde, Solutal Marangoni flow as the cause of ring stains from drying salty colloidal drops, *Physical Review Fluids* 4 (4). doi:10.1103/PhysRevFluids.4.041601.
- [45] M. Cachile, M. Schneemilch, A. Hamraoui, A. Cazabat, Films driven by surface tension gradients, *Advances in Colloid and Interface Science* 96 (1) (2002) 59–74, a Collection of Papers in Honour of Nikolay Churaev on the Occasion of his 80th Birthday. doi:10.1016/S0001-8686(01)00075-6.
- [46] D. V. Zaitsev, O. A. Kabov, An experimental modeling of gravity effect on rupture of a locally heated liquid film, *Microgravity Science and Technology* 19 (3) (2007) 174–177. doi:10.1007/BF02915791.
- [47] J. G. Leidenfrost, De Aquae Communis Nonnullis Qualitatibus Tractatus, Okenius, 1756.
- [48] O. A. Kabov, D. V. Zaitsev, D. P. Kirichenko, V. S. Ajaev, Interaction of levitating microdroplets with moist air flow in the contact line region, *Nanoscale and Microscale Thermophysical Engineering* 21 (2) (2017) 60–69. doi:10.1080/15567265.2017.1279249.
- [49] C. Kruse, I. Somanas, T. Anderson, C. Wilson, C. Zuhlke, D. Alexander, G. Gogos, S. Ndao, Self-propelled droplets on heated surfaces with angled self-assembled micro/nanostructures, *Microfluidics and nanofluidics* 18 (5-6) (2015) 1417–1424. doi:10.1007/s10404-014-1540-6.
- [50] D. V. Zaitsev, D. P. Kirichenko, V. S. Ajaev, O. A. Kabov, Levitation and self-organization of liquid microdroplets over dry heated substrates, *Phys. Rev. Lett.* 119 (2017) 094503. doi:10.1103/PhysRevLett.119.094503.
- [51] R. V. Craster, O. K. Matar, Dynamics and stability of thin liquid films, *Rev. Mod. Phys.* 81 (2009) 1131–1198. doi:10.1103/RevModPhys.81.1131.
- [52] A. B. Afsar-Siddiqui, P. F. Luckham, O. K. Matar, The spreading of surfactant solutions on thin liquid films, *Advances in Colloid and Interface Science* 106 (1-3) (2003) 183–236. doi:10.1016/s0001-8686(03)00111-8.
- [53] Y. Y. Tarasevich, Mechanisms and models of the dehydration self-organization in biological fluids, *Phys. Usp.* 47 (7) (2004) 717–728. doi:10.1070/PU2004v047n07ABEH001758.
- [54] T. A. Yakhno, V. G. Yakhno, Structural evolution of drying drops of biological fluids, *Technical Physics* 54 (8) (2009) 1219–1227. doi:10.1134/S1063784209080210.
- [55] B. S. Sikarwar, S. Khandekar, S. Agrawal, S. Kumar, K. Muralidhar, Dropwise condensation studies on multiple scales, *Heat Transfer Engineering* 33 (4-5) (2012) 301–341. doi:10.1080/01457632.2012.

- 611463.
- [56] D. Bonn, J. Eggers, J. Indekeu, J. Meunier, E. Rolley, Wetting and spreading, *Reviews of Modern Physics* 81 (2) (2009) 739–805. doi:10.1103/revmodphys.81.739.
  - [57] M. Edalatpour, L. Liu, A. Jacobi, K. Eid, A. Sommers, Managing water on heat transfer surfaces: A critical review of techniques to modify surface wettability for applications with condensation or evaporation, *Applied Energy* 222 (2018) 967–992. doi:https://doi.org/10.1016/j.apenergy.2018.03.178.
  - [58] B. Bhushan, Y. C. Jung, Natural and biomimetic artificial surfaces for superhydrophobicity, self-cleaning, low adhesion, and drag reduction, *Progress in Materials Science* 56 (1) (2011) 1–108. doi:https://doi.org/10.1016/j.pmatsci.2010.04.003.
  - [59] W. Han, Z. Lin, Learning from “coffee rings”: Ordered structures enabled by controlled evaporative self-assembly, *Angewandte Chemie International Edition* 51 (7) (2012) 1534–1546. doi:10.1002/anie.201104454.
  - [60] M. Parsa, S. Harmand, K. Sefiane, Mechanisms of pattern formation from dried sessile drops, *Advances in Colloid and Interface Science* 254 (2018) 22–47. doi:10.1016/j.cis.2018.03.007.
  - [61] N. D. Patil, R. Bhardwaj, Recent developments on colloidal deposits obtained by evaporation of sessile droplets on a solid surface, *Journal of the Indian Institute of Science* 99 (1) (2019) 143–156. doi:10.1007/s41745-019-0105-9.
  - [62] A. F. Routh, Drying of thin colloidal films, *Reports on Progress in Physics* 76 (4) (2013) 046603. doi:10.1088/0034-4885/76/4/046603.
  - [63] T. Brugarolas, F. Tu, D. Lee, Directed assembly of particles using microfluidic droplets and bubbles, *Soft Matter* 9 (38) (2013) 9046–9058. doi:10.1039/c3sm50888a.
  - [64] N. M. Kovalchuk, A. Trybala, V. M. Starov, Evaporation of sessile droplets, *Current Opinion in Colloid & Interface Science* 19 (4) (2014) 336–342. doi:10.1016/j.cocis.2014.07.005.
  - [65] H. Hu, R. G. Larson, Drying a sessile droplet: imaging and analysis of transport and deposition patterns, in: *Evaporative Self-Assembly of Ordered Complex Structures*, World Scientific, 2012, pp. 1–57. doi:10.1142/9789814304696\_0001.
  - [66] D. Zang, S. Tarafdar, Y. Y. Tarasevich, M. D. Choudhury, T. Dutta, Evaporation of a droplet: From physics to applications, *Physics Reports* doi:10.1016/j.physrep.2019.01.008.
  - [67] H. Y. Erbil, Control of stain geometry by drop evaporation of surfactant containing dispersions, *Adv. Colloid Interface Sci.* 222 (2015) 275–290. doi:10.1016/j.cis.2014.08.004.
  - [68] X. Zhong, A. Crivoi, F. Duan, Sessile nanofluid droplet drying, *Advances in Colloid and Interface Science* 217 (2015) 13–30. doi:10.1016/j.cis.2014.12.003.
  - [69] T. Gambaryan-Roisman, Modulation of marangoni convection in liquid films, *Advances in Colloid and Interface Science* 222 (2015) 319–331. doi:10.1016/j.cis.2015.02.003.
  - [70] S. I. Karakashev, E. D. Manev, Hydrodynamics of thin liquid films: Retrospective and perspectives, *Advances in Colloid and Interface Science* 222 (2015) 398–412. doi:10.1016/j.cis.2014.07.010.
  - [71] E. Bormashenko, Liquid marbles, elastic nonstick droplets: From minireactors to self-propulsion, *Langmuir* 33 (3) (2016) 663–669. doi:10.1021/acs.langmuir.6b03231.
  - [72] V. S. Ajaev, O. A. Kabov, Heat and mass transfer near contact lines on heated surfaces, *International Journal of Heat and Mass Transfer* 108 (2017) 918–932. doi:10.1016/j.ijheatmasstransfer.2016.11.079.
  - [73] V. Lotito, T. Zambelli, Approaches to self-assembly of colloidal monolayers: A guide for nanotechnologists, *Advances in Colloid and Interface Science* 246 (2017) 217–274. doi:10.1016/j.cis.2017.04.003.
  - [74] K. N. Al-Milaji, H. Zhao, New perspective of mitigating the coffee-ring effect: Interfacial assembly, *The Journal of Physical Chemistry C* 123 (19) (2019) 12029–12041. doi:10.1021/acs.jpcc.9b00797.
  - [75] D. Brutin, V. Starov, Recent advances in droplet wetting and evaporation, *Chem. Soc. Rev.* 47 (2) (2018) 558–585. doi:10.1039/c6cs00902f.
  - [76] S. Tarafdar, Y. Y. Tarasevich, M. Dutta Choudhury, T. Dutta, D. Zang, Droplet drying patterns on solid substrates: From hydrophilic to superhydrophobic contact to levitating drops, *Adv. Condens. Matter Phys.* 2018. doi:10.1155/2018/5214924.
  - [77] F. Giorgetti-Dauphiné, L. Pauchard, Drying drops, *Eur. Phys. J. E* 41 (3) (2018) 32. doi:10.1140/epje/i2018-11639-2.
  - [78] R. Wen, X. Ma, Y.-C. Lee, R. Yang, Liquid-vapor phase-change heat transfer on functionalized nanowired surfaces and beyond, *Joule* 2 (11) (2018) 2307–2347. doi:10.1016/j.joule.2018.08.014.
  - [79] M. Schulz, J. L. Keddie, A critical and quantitative review of the stratification of particles during the drying of colloidal films, *Soft Matter* 14 (2018) 6181–6197. doi:10.1039/C8SM01025K.
  - [80] B. B. Patel, Y. Diao, Multiscale assembly of solution-processed organic electronics: the critical roles of confinement, fluid flow, and interfaces, *Nanotechnology* 29 (4) (2018) 044004. doi:10.1088/1361-6528/aa9d7c.
  - [81] P. E. Theodorakis, E. R. Smith, R. V. Craster, E. A. Müller, O. K. Matar, Molecular dynamics simulation of the superspreading of surfactant-laden droplets. A review, *Fluids* 4 (4) (2019) 176. doi:10.3390/fluids4040176.
  - [82] X. Shao, F. Duan, Y. Hou, X. Zhong, Role of surfactant in controlling the deposition pattern of a particle-laden droplet: Fundamentals and strategies, *Advances in Colloid and Interface Science* 275 (2020) 102049. doi:10.1016/j.cis.2019.102049.
  - [83] Z. Lin, Evaporative self-assembly of ordered complex structures, *World Scientific*, 2012. doi:10.1142/7729.
  - [84] P. Innocenzi, L. Malfatti, P. Falcato, *Water droplets to nanotechnology*, Royal Society of Chemistry, 2013. URL <https://pubs.rsc.org/en/content/ebook/978-1-84973-664-0>
  - [85] S. Sazhin, *Droplets and sprays*, Vol. 220, Springer, 2014. doi:10.1007/978-1-4471-6386-2.
  - [86] D. Brutin, *Droplet wetting and evaporation: from pure to complex fluids*, Academic Press, 2015. doi:10.1016/C2013-0-18955-6.
  - [87] L. Goehring, A. Nakahara, T. Dutta, S. Kitsunezaki, S. Tarafdar, *Desiccation cracks and their patterns: Formation and Modelling in Science and Nature*, John Wiley & Sons, 2015.
  - [88] R. van Dommelen, P. Fanzio, L. Sasso, Surface self-assembly of colloidal crystals for micro- and nano-patterning, *Advances in Colloid and Interface Science* 251 (2018) 97–114. doi:10.1016/j.cis.2017.10.007.
  - [89] G. J. de A. A. Soler-Illia, A. Louis, C. Sanchez, Synthesis and characterization of mesostructured titania-based materials through evaporation-induced self-assembly, *Chemistry of Materials* 14 (2) (2002) 750–759. doi:10.1021/cm011217a.
  - [90] C. J. Brinker, Evaporation-induced self-assembly: Functional nanostructures made easy, *MRS Bulletin* 29 (9) (2004) 631–640. doi:10.1557/mrs2004.183.
  - [91] D. Grosso, F. Cagnol, G. Soler-Illia, E. Crepaldi, H. Amenitsch, A. Brunet-Bruneau, A. Bourgeois, C. Sanchez, Fundamentals of mesostructuring through evaporation-induced self-assembly, *Advanced Functional Materials* 14 (4) (2004) 309–322. doi:10.1002/adfm.200305036.
  - [92] E. Bormashenko, R. Pogreb, O. Stanevsky, Y. Bormashenko, T. Stein, O. Gengelman, Mesoscopic patterning in evaporated polymer solutions: New experimental data and physical mechanisms, *Langmuir* 21 (21) (2005) 9604–9609. doi:10.1021/la0518492.
  - [93] X. Li, C. Wang, J. Shao, Y. Ding, H. Tian, X. Li, L. Wang, Periodic parallel array of nanopillars and nanoholes resulting from colloidal stripes patterned by geometrically confined evaporative self-assembly for unique anisotropic wetting, *ACS Applied Materials & Interfaces* 6 (22) (2014) 20300–20308. doi:10.1021/am505835z.
  - [94] M. A. Jabal, A. Egbaria, A. Zigelman, U. Thiele, O. Manor, Connecting monotonic and oscillatory motions of the meniscus of a volatile polymer solution to the transport of polymer coils and deposit morphology, *Langmuir* 34 (39) (2018) 11784–11794. doi:10.1021/acs.langmuir.8b02268.
  - [95] X. Li, X. Zhu, H. Wei, Microstructure formation of functional polymers by evaporative self-assembly under flexible geometric confinement, *Micromachines* 9 (3) (2018) 124. doi:10.3390/mi9030124.
  - [96] J. Xu, J. Xia, S. W. Hong, Z. Lin, F. Qiu, Y. Yang, Self-assembly of gradient concentric rings via solvent evaporation from a capillary bridge, *Phys. Rev. Lett.* 96 (2006) 066104. doi:10.1103/PhysRevLett.96.



066104.

- [97] J. Xu, J. Xia, Z. Lin, Evaporation-induced self-assembly of nanoparticles from a sphere-on-flat geometry, *Angewandte Chemie International Edition* 46 (11) (2007) 1860–1863. doi:10.1002/anie.200604540.
- [98] B. Li, W. Han, M. Byun, L. Zhu, Q. Zou, Z. Lin, Macroscopic highly aligned DNA nanowires created by controlled evaporative self-assembly, *ACS Nano* 7 (5) (2013) 4326–4333. doi:10.1021/nn400840y.
- [99] S. W. Hong, M. Byun, Z. Lin, Robust self-assembly of highly ordered complex structures by controlled evaporation of confined microfluids, *Angewandte Chemie International Edition* 48 (3) (2009) 512–516. doi:10.1002/anie.200804633.
- [100] S. Li, Y. T. Chun, S. Zhao, H. Ahn, D. Ahn, J. I. Sohn, Y. Xu, P. Shrestha, M. Pivnenko, D. Chu, High-resolution patterning of solution-processable materials via externally engineered pinning of capillary bridges, *Nature Communications* 9 (1). doi:10.1038/s41467-018-02835-7.
- [101] X. Li, J. Shao, X. Zhu, H. Wei, Mwcnts patterning by thermally enhanced and confined evaporation for transparent and conductive thin film, *Modern Physics Letters B* 32 (29) (2018) 1850360. doi:10.1142/S0217984918503608.
- [102] H. Li, T. C. Hain, A. Muzha, F. Schöppler, T. Hertel, Dynamical contact line pinning and zipping during carbon nanotube coffee stain formation, *ACS Nano* 8 (6) (2014) 6417–6424. doi:10.1021/nm501957y.
- [103] M. He, B. Li, X. Cui, B. Jiang, Y. He, Y. Chen, D. O’Neil, P. Szymanski, M. A. El-Sayed, J. Huang, Z. Lin, Meniscus-assisted solution printing of large-grained perovskite films for high-efficiency solar cells, *Nature Communications* 8 (2017) 16045. doi:10.1038/ncomms16045.
- [104] S. Das, E.-S. M. Duraia, O. D. Velez, M. D. Amiri, G. W. Beall, Formation of periodic size-segregated stripe pattern via directed self-assembly of binary colloids and its mechanism, *Applied Surface Science* 435 (2018) 512–520. doi:10.1016/j.apsusc.2017.11.142.
- [105] S. Choudhary, A. J. Crosby, Controlled evaporative self-assembly of polymer nanoribbons using oscillating capillary bridges, *Journal of Polymer Science Part B: Polymer Physics* 56 (23) (2018) 1545–1551. doi:10.1002/polb.24730.
- [106] H. Bodiguel, F. Doumenc, B. Guerrier, Pattern formation during the drying of a colloidal suspension, *The European Physical Journal Special Topics* 166 (1) (2009) 29–32. doi:10.1140/epjst/e2009-00873-3.
- [107] H. Bodiguel, F. Doumenc, B. Guerrier, Stick-slip patterning at low capillary numbers for an evaporating colloidal suspension, *Langmuir* 26 (13) (2010) 10758–10763. doi:10.1021/la100547j.
- [108] A. Dong, J. Chen, S. J. Oh, W. kyu Koh, F. Xiu, X. Ye, D.-K. Ko, K. L. Wang, C. R. Kagan, C. B. Murray, Multiscale periodic assembly of striped nanocrystal superlattice films on a liquid surface, *Nano Letters* 11 (2) (2011) 841–846. doi:10.1021/nl104208x.
- [109] H. Nakamura, *Colloidal crystals*, R&D Review of Toyota CRDL 39 (4) (2004) 33–39. URL [https://www.tytlabs.com/japanese/review/rev394pdf/394\\_033nakamura.pdf](https://www.tytlabs.com/japanese/review/rev394pdf/394_033nakamura.pdf)
- [110] G. Lozano, H. Míguez, Growth dynamics of self-assembled colloidal crystal thin films, *Langmuir* 23 (20) (2007) 9933–9938. doi:10.1021/la701737v.
- [111] H. Cao, D. Lan, Y. Wang, A. A. Volinsky, L. Duan, H. Jiang, Fracture of colloidal single-crystal films fabricated by controlled vertical drying deposition, *Physical Review E* 82 (3). doi:10.1103/physreve.82.031602.
- [112] C. Zhang, X. Zhang, X. Zhang, X. Fan, J. Jie, J. C. Chang, C.-S. Lee, W. Zhang, S.-T. Lee, Facile one-step growth and patterning of aligned squaraine nanowires via evaporation-induced self-assembly, *Advanced Materials* 20 (9) (2008) 1716–1720. doi:10.1002/adma.200703142.
- [113] J. Li, B. Cabane, M. Sztucki, J. Gummel, L. Goehring, Drying dip-coated colloidal films, *Langmuir* 28 (1) (2011) 200–208. doi:10.1021/la203549g.
- [114] D. Grosso, How to exploit the full potential of the dip-coating process to better control film formation, *Journal of Materials Chemistry* 21 (43) (2011) 17033. doi:10.1039/c1jm12837j.
- [115] J. Jang, S. Nam, K. Im, J. Hur, S. N. Cha, J. Kim, H. B. Son, H. Suh, M. A. Loth, J. E. Anthony, J.-J. Park, C. E. Park, J. M. Kim, K. Kim, Highly crystalline soluble acene crystal arrays for organic transistors: Mechanism of crystal growth during dip-coating, *Advanced Functional Materials* 22 (5) (2012) 1005–1014. doi:10.1002/adfm.201102284.
- [116] S. Lenhart, L. Zhang, J. Mueller, H. Wiesmann, G. Erker, H. Fuchs, L. Chi, Self-organized complex patterning: Langmuir–blodgett lithography, *Advanced Materials* 16 (7) (2004) 619–624. doi:10.1002/adma.200306203.
- [117] X. Chen, N. Lu, H. Zhang, M. Hirtz, L. Wu, H. Fuchs, L. Chi, Langmuir–blodgett patterning of phospholipid microstripes: Effect of the second component, *The Journal of Physical Chemistry B* 110 (15) (2006) 8039–8046. doi:10.1021/jp0602530.
- [118] U. Thiele, I. Vancea, A. J. Archer, M. J. Robbins, L. Frastia, A. Stannard, E. Pauliac-Vaujour, C. P. Martin, M. O. Blunt, P. J. Moriarty, Modelling approaches to the dewetting of evaporating thin films of nanoparticle suspensions, *Journal of Physics: Condensed Matter* 21 (26) (2009) 264016. doi:10.1088/0953-8984/21/26/264016.
- [119] A. Stannard, Dewetting-mediated pattern formation in nanoparticle assemblies, *Journal of Physics: Condensed Matter* 23 (8) (2011) 083001. doi:10.1088/0953-8984/23/8/083001.
- [120] W. Li, D. Lan, Y. Wang, Dewetting-mediated pattern formation inside the coffee ring, *Physical Review E* 95 (4). doi:10.1103/physreve.95.042607.
- [121] U. Thiele, Patterned deposition at moving contact lines, *Adv. Colloid Interface Sci.* 206 (2014) 399–413. doi:10.1016/j.cis.2013.11.002.
- [122] S. J. S. Morris, A phenomenological model for the contact region of an evaporating meniscus on a superheated slab, *Journal of Fluid Mechanics* 411 (2000) 59–89. doi:10.1017/s0022112099008046.
- [123] S. J. S. Morris, Contact angles for evaporating liquids predicted and compared with existing experiments, *Journal of Fluid Mechanics* 432 (2001) 1–30. doi:10.1017/s0022112000003074.
- [124] S. J. S. Morris, On the contact region of a diffusion-limited evaporating drop: a local analysis, *Journal of Fluid Mechanics* 739 (2014) 308–337. doi:10.1017/jfm.2013.577.
- [125] A. Rednikov, P. Colinet, Singularity-free description of moving contact lines for volatile liquids, *Phys. Rev. E* 87 (2013) 010401. doi:10.1103/PhysRevE.87.010401.
- [126] A. Y. Rednikov, P. Colinet, Asymptotic analysis of the contact-line microregion for a perfectly wetting volatile liquid in a pure-vapor atmosphere, *Physical Review Fluids* 2 (12). doi:10.1103/physrevfluids.2.124006.
- [127] A. Y. Rednikov, P. Colinet, Contact-line singularities resolved exclusively by the kelvin effect: volatile liquids in air, *Journal of Fluid Mechanics* 858 (2019) 881–916. doi:10.1017/jfm.2018.760.
- [128] M. R. E. Warner, R. V. Craster, O. K. Matar, Surface patterning via evaporation of ultrathin films containing nanoparticles, *Journal of Colloid and Interface Science* 267 (1) (2003) 92–110. doi:10.1016/s0021-9797(03)00640-4.
- [129] Y. Liang, N. Hilal, P. Langston, V. Starov, Interaction forces between colloidal particles in liquid: Theory and experiment, *Advances in Colloid and Interface Science* 134–135 (2007) 151–166. doi:10.1016/j.cis.2007.04.003.
- [130] N. Kovalchuk, D. Johnson, V. Sobolev, N. Hilal, V. Starov, Interactions between nanoparticles in nanosuspension, *Advances in Colloid and Interface Science* 272 (2019) 102020. doi:10.1016/j.cis.2019.102020.
- [131] S. P. Molchanov, V. I. Roldughin, I. A. Chernova-Kharaeva, I. N. Senchikhin, The effect of electrokinetic potential on evaporation of colloidal dispersion droplets, *Colloid Journal* 81 (2) (2019) 136–145. doi:10.1134/s1061933x19020091.
- [132] N. D. Denkov, O. D. Velez, P. A. Kralchevsky, I. B. Ivanov, H. Yoshimura, K. Nagayama, Two-dimensional crystallization, *Nature* 361 (6407) (1993) 26–26. doi:10.1038/361026a0.
- [133] P. A. Kralchevsky, K. Nagayama, Capillary forces between colloidal particles, *Langmuir* 10 (1) (1994) 23–36. doi:10.1021/la00013a004.
- [134] B. J. Park, E. M. Furst, Attractive interactions between colloids at the oil–water interface, *Soft Matter* 7 (17) (2011) 7676. doi:10.1039/c1sm00005e.
- [135] N. Denkov, O. Velez, P. Kralchevsky, I. Ivanov, H. Yoshimura, K. Nagayama, Mechanism of formation of two-dimensional crystals from latex particles on substrates, *Langmuir* 8 (12) (1992) 3183–3190. doi:10.1021/la00048a054.
- [136] S. Liu, T. Zhu, R. Hu, Z. Liu, Evaporation-induced self-assembly of gold nanoparticles into a highly organized two-dimensional array, *Physical*

- Chemistry Chemical Physics 4 (24) (2002) 6059–6062. doi:10.1039/b208520h.
- [137] W. Li, W. Ji, D. Lan, Y. Wang, Self-assembly of ordered microparticle monolayers from drying a droplet on a liquid substrate, *The Journal of Physical Chemistry Letters* 10 (20) (2019) 6184–6188. doi:10.1021/acs.jpcllett.9b01917.
- [138] P. Qiu, C. Jensen, N. Charity, R. Towner, C. Mao, Oil phase evaporation-induced self-assembly of hydrophobic nanoparticles into spherical clusters with controlled surface chemistry in an oil-in-water dispersion and comparison of behaviors of individual and clustered iron oxide nanoparticles, *Journal of the American Chemical Society* 132 (50) (2010) 17724–17732. doi:10.1021/ja102138a.
- [139] Y. Wang, G. W. Padua, Nanoscale characterization of zein self-assembly, *Langmuir* 28 (5) (2012) 2429–2435. doi:10.1021/la204204j.
- [140] J. Wang, Q. Cheng, L. Lin, L. Jiang, Synergistic toughening of bioinspired poly(vinyl alcohol)–clay–nanofibrillar cellulose artificial nacre, *ACS Nano* 8 (3) (2014) 2739–2745. doi:10.1021/nn406428n.
- [141] G.-H. Lim, K. Ahn, S. Bok, J. Nam, B. Lim, Curving silver nanowires using liquid droplets for highly stretchable and durable percolation networks, *Nanoscale* 9 (26) (2017) 8938–8944. doi:10.1039/c7nr02615c.
- [142] A. F. Routh, W. B. Russel, Horizontal drying fronts during solvent evaporation from latex films, *AIChE Journal* 44 (9) (1998) 2088–2098. doi:10.1002/aic.690440916.
- [143] D. J. Harris, H. Hu, J. C. Conrad, J. A. Lewis, Patterning colloidal films via evaporative lithography, *Physical Review Letters* 98 (14) (2007) 148301. doi:10.1103/PhysRevLett.98.148301.
- [144] J. Aizenberg, P. V. Braun, P. Wiltzius, Patterned colloidal deposition controlled by electrostatic and capillary forces, *Phys. Rev. Lett.* 84 (2000) 2997–3000. doi:10.1103/PhysRevLett.84.2997.
- [145] H. Zheng, I. Lee, M. Rubner, P. Hammond, Two component particle arrays on patterned polyelectrolyte multilayer templates, *Advanced Materials* 14 (8) (2002) 569–572. doi:10.1002/1521-4095(20020418)14:8<569::AID-ADMA569>3.0.CO;2-O.
- [146] A. van Blaaderen, R. Ruel, P. Wiltzius, Template-directed colloidal crystallization, *Nature* 385 (6614) (1997) 321–324. doi:10.1038/385321a0.
- [147] K.-h. Lin, J. C. Crocker, V. Prasad, A. Schofield, D. A. Weitz, T. C. Lubensky, A. G. Yodh, Entropically driven colloidal crystallization on patterned surfaces, *Phys. Rev. Lett.* 85 (2000) 1770–1773. doi:10.1103/PhysRevLett.85.1770.
- [148] W. Lee, A. Chan, M. A. Bevan, J. A. Lewis, P. V. Braun, Nanoparticle-mediated epitaxial assembly of colloidal crystals on patterned substrates, *Langmuir* 20 (13) (2004) 5262–5270. doi:10.1021/la035694e.
- [149] A. Malainou, K. Tsougeni, K. Ellinas, P. S. Petrou, V. Constantoudis, E. Sarantopoulou, K. Awsiuk, A. Bernasik, A. Budkowski, A. Markou, I. Panagiotopoulos, S. E. Kakabakos, E. Gogolides, A. Tserepi, Plasma-assisted nanoscale protein patterning on si substrates via colloidal lithography, *The Journal of Physical Chemistry A* 117 (50) (2013) 13743–13751. doi:10.1021/jp407810x.
- [150] M. Yasuda, K. Tada, Y. Hirai, Molecular dynamics study on mold and pattern breakages in nanoimprint lithography, in: M. Wang (Ed.), *Lithography, InTech*, 2010, pp. 543–556. doi:10.5772/8192.
- [151] W. M. Moreau, *Semiconductor lithography: principles, practices, and materials*, Springer Science & Business Media, 1988. doi:10.1007/978-1-4613-0885-0.
- [152] S. H. Kim, J. H. Jeong, J. R. Youn, Nanopattern insert molding, *Nanotechnology* 21 (20) (2010) 205302. doi:10.1088/0957-4484/21/20/205302.
- [153] E. Kim, Y. Xia, G. M. Whitesides, Polymer microstructures formed by moulding in capillaries, *Nature* 376 (6541) (1995) 581–584. doi:10.1038/376581a0.
- [154] S. Jeon, J.-W. Kang, H.-D. Park, J.-J. Kim, J. R. Youn, J. Shim, J.-h. Jeong, D.-G. Choi, K.-D. Kim, A. O. Altun, S.-H. Kim, Y.-H. Lee, Ultraviolet nanoimprinted polymer nanostructure for organic light emitting diode application, *Applied Physics Letters* 92 (22) (2008) 223307. doi:10.1063/1.2939554.
- [155] J.-R. Li, K. L. Lusker, J.-J. Yu, J. C. Garno, Engineering the spatial selectivity of surfaces at the nanoscale using particle lithography combined with vapor deposition of organosilanes, *ACS Nano* 3 (7) (2009) 2023–2035. doi:10.1021/nn9004796.
- [156] J.-R. Li, J. C. Garno, Nanostructures of octadecyltrisiloxane self-assembled monolayers produced on au(111) using particle lithography, *ACS Applied Materials & Interfaces* 1 (4) (2009) 969–976. doi:10.1021/am900118x.
- [157] J. Zhang, Y. Li, X. Zhang, B. Yang, Colloidal self-assembly meets nanofabrication: From two-dimensional colloidal crystals to nanostructure arrays, *Advanced Materials* 22 (38) (2010) 4249–4269. doi:10.1002/adma.201000755.
- [158] F. Pi, P. Dillard, L. Limozin, A. Charrier, K. Sengupta, Nanometric protein-patch arrays on glass and polydimethylsiloxane for cell adhesion studies, *Nano Letters* 13 (7) (2013) 3372–3378. doi:10.1021/nl401696m.
- [159] D. Wu, N. Fang, C. Sun, X. Zhang, Adhesion force of polymeric three-dimensional microstructures fabricated by microstereolithography, *Applied Physics Letters* 81 (21) (2002) 3963–3965. doi:10.1063/1.1522825.
- [160] D. Wu, N. Fang, C. Sun, X. Zhang, Stiction problems in releasing of 3D microstructures and its solution, *Sensors and Actuators A: Physical* 128 (1) (2006) 109–115. doi:10.1016/j.sna.2005.12.041.
- [161] A. Georgiadis, A. F. Routh, M. W. Murray, J. L. Keddie, Bespoke periodic topography in hard polymer films by infrared radiation-assisted evaporative lithography, *Soft Matter* 7 (2011) 11098–11102. doi:10.1039/C1SM06527K.
- [162] H. Zhao, J. Xu, G. Jing, L. O. Prieto-Lopez, X. Deng, J. Cui, Controlling the localization of liquid droplets in polymer matrices by evaporative lithography, *Angewandte Chemie International Edition* 55 (36) (2016) 10681–10685. doi:10.1002/anie.201604868.
- [163] D. J. Harris, J. A. Lewis, Marangoni effects on evaporative lithographic patterning of colloidal films, *Langmuir* 24 (8) (2008) 3681–3685. doi:10.1021/la8000637.
- [164] A. Georgiadis, F. N. Muhamad, A. Utgenannt, J. L. Keddie, Aesthetically textured, hard latex coatings by fast IR-assisted evaporative lithography, *Progress in Organic Coatings* 76 (12) (2013) 1786–1791. doi:10.1016/j.porgcoat.2013.05.017.
- [165] M. Kimura, M. J. Misner, T. Xu, S. H. Kim, T. P. Russell, Long-range ordering of diblock copolymers induced by droplet pinning, *Langmuir* 19 (23) (2003) 9910–9913. doi:10.1021/la0351360.
- [166] L. Chen, J. R. G. Evans, Arched structures created by colloidal droplets as they dry, *Langmuir* 25 (19) (2009) 11299–11301. doi:10.1021/la902918m.
- [167] T. K. Pradhan, P. K. Panigrahi, Deposition pattern of interacting droplets, *Colloids and Surfaces A: Physicochemical and Engineering Aspects* 482 (2015) 562–567. doi:10.1016/j.colsurfa.2015.07.013.
- [168] O. Hegde, S. Chakraborty, P. Kabi, S. Basu, Vapor mediated control of microscale flow in sessile droplets, *Physics of Fluids* 30 (12) (2018) 122103. doi:10.1063/1.5054632.
- [169] O. Hegde, P. Kabi, S. Agarwal, S. Basu, Controlling self-assembly and buckling in nano fluid droplets through vapour mediated interaction of adjacent droplets, *Journal of Colloid and Interface Science* 541 (2019) 348–355. doi:10.1016/j.jcis.2019.01.106.
- [170] L. K. Malla, R. Bhardwaj, A. Neild, Colloidal deposit of an evaporating sessile droplet on a non-uniformly heated substrate, *Colloids and Surfaces A: Physicochemical and Engineering Aspects* (2019) 124009. doi:10.1016/j.colsurfa.2019.124009.
- [171] B. Rieger, L. R. van den Doel, L. J. van Vliet, Ring formation in nanoliter cups: Quantitative measurements of flow in micromachined wells, *Physical Review E* 68 (3) (2003) 036312. doi:10.1103/PhysRevE.68.036312.
- [172] D. J. Harris, J. C. Conrad, J. A. Lewis, Evaporative lithographic patterning of binary colloidal films, *Philosophical Transactions of the Royal Society A: Mathematical, Physical and Engineering Sciences* 367 (1909) (2009) 5157–5165. doi:10.1098/rsta.2009.0157.
- [173] C. Parneix, P. Vandoelaeghe, V. S. Nikolayev, D. Quéré, J. Li, B. Cabane, Dips and rims in dried colloidal films, *Physical Review Letters* 105 (26) (2010) 266103. doi:10.1103/PhysRevLett.105.266103.
- [174] P. Cavadini, J. Krenn, P. Scharfer, W. Schabel, Investigation of surface deformation during drying of thin polymer films due to marangoni convection, *Chemical Engineering and Processing: Process Intensification* 64 (2013) 24–30. doi:10.1016/j.cep.2012.11.008.
- [175] P. Cavadini, J. Erz, D. Sachsenheimer, A. Kowalczyk, N. Willenbacher, P. Scharfer, W. Schabel, Investigation of the flow field in thin polymer films due to inhomogeneous drying, *Journal of Coatings*

- Technology and Research 12 (5) (2015) 921–926. doi:10.1007/s11998-015-9725-9.
- [176] P. Cavadini, H. Weinhold, M. Tönsmann, S. Chilingaryan, A. Kopmann, A. Lewkowicz, C. Miao, P. Scharfer, W. Schabel, Investigation of the flow structure in thin polymer films using 3d  $\mu$ ptv enhanced by gpu, *Experiments in Fluids* 59 (4) (2018) 61. doi:10.1007/s00348-017-2482-z.
- [177] T. M. Yen, X. Fu, T. Wei, R. U. Nayak, Y. Shi, Y.-H. Lo, Reversing coffee-ring effect by laser-induced differential evaporation, *Scientific Reports* 8 (1) (2018) 3157. doi:10.1038/s41598-018-20581-0.
- [178] M. Anyfantakis, S. N. Varanakkottu, S. Rudiuk, M. Morel, D. Baigl, Evaporative optical marangoni assembly: Tailoring the three-dimensional morphology of individual deposits of nanoparticles from sessile drops, *ACS Applied Materials & Interfaces* 9 (42) (2017) 37435–37445. doi:10.1021/acsami.7b11547.
- [179] A. K. Thokchom, A. Gupta, P. J. Jaijuss, A. Singh, Analysis of fluid flow and particle transport in evaporating droplets exposed to infrared heating, *International Journal of Heat and Mass Transfer* 68 (2014) 67–77. doi:10.1016/j.ijheatmasstransfer.2013.09.012.
- [180] A. Askounis, Y. Kita, M. Kohno, Y. Takata, V. Koutsos, K. Sefiane, Influence of local heating on marangoni flows and evaporation kinetics of pure water drops, *Langmuir* 33 (23) (2017) 5666–5674, PMID: 28510453. doi:10.1021/acs.langmuir.7b00957.
- [181] J. A. Vieyra Salas, J. M. van der Veen, J. J. Michels, A. A. Darhuber, Active control of evaporative solution deposition by modulated infrared illumination, *The Journal of Physical Chemistry C* 116 (22) (2012) 12038–12047. doi:10.1021/jp301092y.
- [182] H. M. J. M. Wedershoven, K. R. M. Deuss, C. Fantin, J. C. H. Zeegers, A. A. Darhuber, Active control of evaporative solution deposition by means of modulated gas phase convection, *International Journal of Heat and Mass Transfer* 117 (2018) 303–312. doi:10.1016/j.ijheatmasstransfer.2017.09.123.
- [183] R. Malinowski, G. Volpe, I. P. Parkin, G. Volpe, Dynamic control of particle deposition in evaporating droplets by an external point source of vapor, *The Journal of Physical Chemistry Letters* 9 (3) (2018) 659–664. doi:10.1021/acs.jpclett.7b02831.
- [184] V. D. Ta, R. M. Carter, E. Esenturk, C. Connaughton, T. J. Wasley, J. Li, R. W. Kay, J. Stringer, P. J. Smith, J. D. Shephard, Dynamically controlled deposition of colloidal nanoparticle suspension in evaporating drops using laser radiation, *Soft Matter* 12 (2016) 4530–4536. doi:10.1039/C6SM00465B.
- [185] C. Noirjean, M. Marcellini, S. Deville, T. E. Kodger, C. Monteux, Dynamics and ordering of weakly Brownian particles in directional drying, *Physical Review Materials* 1 (6). doi:10.1103/physrevmaterials.1.065601.
- [186] S. N. Varanakkottu, M. Anyfantakis, M. Morel, S. Rudiuk, D. Baigl, Light-directed particle patterning by evaporative optical marangoni assembly, *Nano Letters* 16 (1) (2015) 644–650. doi:10.1021/acs.nanolett.5b04377.
- [187] S. Lone, J. M. Zhang, I. U. Vakarelski, E. Q. Li, S. T. Thoroddsen, Evaporative lithography in open microfluidic channel networks, *Langmuir* 33 (11) (2017) 2861–2871. doi:10.1021/acs.langmuir.6b03304.
- [188] H. K. Park, Y. Kim, H. Min, C. Pang, B. M. Weon, Hexagonal deposits of colloidal particles, *Physical Review E* 100 (2). doi:10.1103/physreve.100.022602.
- [189] I. U. Vakarelski, D. Y. C. Chan, T. Nonoguchi, H. Shinto, K. Higashitani, Assembly of gold nanoparticles into microwire networks induced by drying liquid bridges, *Physical Review Letters* 102 (5). doi:10.1103/physrevlett.102.058303.
- [190] I. U. Vakarelski, J. W. Kwek, X. Tang, S. J. O'Shea, D. Y. C. Chan, Particulate templates and ordered liquid bridge networks in evaporative lithography, *Langmuir* 25 (23) (2009) 13311–13314. doi:10.1021/la9033723.
- [191] I. U. Vakarelski, J. O. Marston, S. T. Thoroddsen, Foam-film-stabilized liquid bridge networks in evaporative lithography and wet granular matter, *Langmuir* 29 (16) (2013) 4966–4973. doi:10.1021/la400662n.
- [192] X. Tang, S. J. O'Shea, I. U. Vakarelski, Photoresist templates for wafer-scale defect-free evaporative lithography, *Advanced Materials* 22 (45) (2010) 5150–5153. doi:10.1002/adma.201002644.
- [193] J. Chen, W.-S. Liao, X. Chen, T. Yang, S. E. Wark, D. H. Son, J. D. Batteas, P. S. Cremer, Evaporation-induced assembly of quantum dots into nanorings, *ACS Nano* 3 (1) (2009) 173–180. doi:10.1021/nn800568t.
- [194] H. M. J. M. Wedershoven, J. C. H. Zeegers, A. A. Darhuber, Polymer film deposition from a receding solution meniscus: The effect of laminar forced air convection, *Chemical Engineering Science* 181 (2018) 92–100. doi:10.1016/j.ces.2018.02.006.
- [195] H. B. Eral, D. M. Augustine, M. H. G. Duits, F. Mugele, Suppressing the coffee stain effect: how to control colloidal self-assembly in evaporating drops using electrowetting, *Soft Matter* 7 (10) (2011) 4954. doi:10.1039/c1sm05183k.
- [196] E. Josten, E. Wetterskog, A. Glavic, P. Boesecke, A. Feoktystov, E. Brauweiler-Reuters, U. Rcker, G. Salazar-Alvarez, T. Brckel, L. Bergström, Superlattice growth and rearrangement during evaporation-induced nanoparticle self-assembly, *Scientific Reports* 7 (1). doi:10.1038/s41598-017-02121-4.
- [197] A. Darras, N. Vandewalle, G. Lumay, Combined effects of Marangoni, sedimentation and coffee-ring flows on evaporative deposits of superparamagnetic colloids, *Colloid and Interface Science Communications* 32 (2019) 100198. doi:10.1016/j.colcom.2019.100198.
- [198] S. K. Saroj, P. K. Panigrahi, Drying pattern and evaporation dynamics of sessile ferrofluid droplet on a PDMS substrate, *Colloids and Surfaces A: Physicochemical and Engineering Aspects* 580 (2019) 123672. doi:10.1016/j.colsurfa.2019.123672.
- [199] K. N. Al-Milaji, R. L. Hadimani, S. Gupta, V. K. Pecharsky, H. Zhao, Inkjet printing of magnetic particles toward anisotropic magnetic properties, *Scientific Reports* 9 (1). doi:10.1038/s41598-019-52699-0.
- [200] O. V. Rudenko, A. I. Korobov, B. A. Korshak, P. V. Lebedev-Stepanov, S. P. Molchanov, M. V. Alfimov, Self-assembly of colloidal-particle ensembles in an acoustic field, *Nanotechnologies in Russia* 5 (7-8) (2010) 469–473. doi:10.1134/s1995078010070062.
- [201] W. Li, W. Ji, H. Sun, D. Lan, Y. Wang, Pattern formation in drying sessile and pendant droplet: Interactions of gravity settling, interface shrinkage, and capillary flow, *Langmuir* 35 (1) (2018) 113–119. doi:10.1021/acs.langmuir.8b02659.
- [202] E. N. Hoggan, D. Flowers, K. Wang, J. M. DeSimone, R. G. Carbonell, Spin coating of photoresists using liquid carbon dioxide, *Industrial & Engineering Chemistry Research* 43 (9) (2004) 2113–2122. doi:10.1021/ie0308543.
- [203] L. Huang, Z. Jia, I. Kyriassis, S. O'Brien, High K Capacitors and OFET gate dielectrics from self-assembled BaTiO<sub>3</sub> and (ba, sr)TiO<sub>3</sub> nanocrystals in the superparaelectric limit, *Advanced Functional Materials* 20 (4) (2010) 554–560. doi:10.1002/adfm.200901258.
- [204] D. Mampallil, M. Sharma, A. Sen, S. Sinha, Beyond the coffee-ring effect: Pattern formation by wetting and spreading of drops, *Physical Review E* 98 (4). doi:10.1103/PhysRevE.98.043107.
- [205] S. K. Saroj, P. K. Panigrahi, Effect of salt concentration (NaCl) on drying pattern of ferrofluid droplets, *Journal of Flow Visualization and Image Processing* 25 (3-4) (2018) 245–258. doi:10.1615/jflowvisimageproc.2018027805.
- [206] H. Sun, W. Li, W. Ji, G. Dai, Y. Huan, Y. Wang, D. Lan, The evaporation of the saline colloidal droplet and the deposition pattern, *Chinese Physics B* doi:10.1088/1674-1056/ab5782.
- [207] E. Homede, O. Manor, Deposition of nanoparticles from a volatile carrier liquid, *Journal of Colloid and Interface Science* 562 (2020) 102–111. doi:10.1016/j.jcis.2019.11.062.
- [208] Z. Zhang, X. Zhang, Z. Xin, M. Deng, Y. Wen, Y. Song, Controlled inkjetting of a conductive pattern of silver nanoparticles based on the coffee-ring effect, *Advanced Materials* 25 (46) (2013) 6714–6718. doi:10.1002/adma.201303278.
- [209] M. Layani, R. Berman, S. Magdassi, Printing holes by a dewetting solution enables formation of a transparent conductive film, *ACS Applied Materials & Interfaces* 6 (21) (2014) 18668–18672. doi:10.1021/am504106s.
- [210] J. Lim, W. Lee, D. Kwak, K. Cho, Evaporation-induced self-organization of inkjet-printed organic semiconductors on surface-modified dielectrics for high-performance organic transistors, *Langmuir* 25 (9) (2009) 5404–5410. doi:10.1021/la804269q.
- [211] A. D. Eales, N. Dartnell, S. Goddard, A. F. Routh, The impact of trough geometry on film shape. A theoretical study of droplets containing polymer, for P-OLED display applications, *Journal of Colloid and Interface Science* 458 (2015) 53–61. doi:10.1016/j.jcis.2015.07.036.



- [212] Y. Park, Y. Park, J. Lee, C. Lee, Simulation for forming uniform inkjet-printed quantum dot layer, *Journal of Applied Physics* 125 (6) (2019) 065304. [doi:10.1063/1.5079863](#).
- [213] C. Jiang, Z. Zhong, B. Liu, Z. He, J. Zou, L. Wang, J. Wang, J. Peng, Y. Cao, Coffee-ring-free quantum dot thin film using inkjet printing from a mixed-solvent system on modified ZnO transport layer for light-emitting devices, *ACS Applied Materials & Interfaces* 8 (39) (2016) 26162–26168, PMID: 27608850. [doi:10.1021/acsami.6b08679](#).
- [214] H. Deng, D. Dong, K. Qiao, L. Bu, B. Li, D. Yang, H.-E. Wang, Y. Cheng, Z. Zhao, J. Tang, H. Song, Growth, patterning and alignment of organolead iodide perovskite nanowires for optoelectronic devices, *Nanoscale* 7 (9) (2015) 4163–4170. [doi:10.1039/c4nr06982j](#).
- [215] M. Layani, M. Gruchko, O. Milo, I. Balberg, D. Azulay, S. Magdassi, Transparent conductive coatings by printing coffee ring arrays obtained at room temperature, *ACS Nano* 3 (11) (2009) 3537–3542. [doi:10.1021/nn901239z](#).
- [216] A. Shimoni, S. Azoubel, S. Magdassi, Inkjet printing of flexible high-performance carbon nanotube transparent conductive films by “coffee ring effect”, *Nanoscale* 6 (19) (2014) 11084–11089. [doi:10.1039/c4nr02133a](#).
- [217] M. Layani, S. Magdassi, Flexible transparent conductive coatings by combining self-assembly with sintering of silver nanoparticles performed at room temperature, *Journal of Materials Chemistry* 21 (39) (2011) 15378. [doi:10.1039/c1jm13174e](#).
- [218] X. Wang, G. Kang, B. Seong, I. Chae, H. T. Yudiantira, H. Lee, H. Kim, D. Byun, Transparent arrays of silver nanowire rings driven by evaporation of sessile droplets, *Journal of Physics D: Applied Physics* 50 (45) (2017) 455302. [doi:10.1088/1361-6463/aa8c23](#).
- [219] A. Utgenannt, J. L. Keddle, O. L. Muskens, A. G. Kanaras, Directed organization of gold nanoparticles in polymer coatings through infrared-assisted evaporative lithography, *Chemical Communications* 49 (39) (2013) 4253–4255. [doi:10.1039/c2cc37844b](#).
- [220] A. Utgenannt, R. Maspero, A. Fortini, R. Turner, M. Florescu, C. Jeynes, A. G. Kanaras, O. L. Muskens, R. P. Sear, J. L. Keddle, Fast assembly of gold nanoparticles in large-area 2D nanogrids using a one-step, near-infrared radiation-assisted evaporation process, *ACS Nano* 10 (2) (2016) 2232–2242. [doi:10.1021/acs.nano.5b06886](#).
- [221] X. Yang, J. Li, Y. Zhao, J. Yang, L. Zhou, Z. Dai, X. Guo, S. Mu, Q. Liu, C. Jiang, M. Sun, J. Wang, W. Liang, Self-assembly of Au@Ag core-shell nanocuboids into staircase superstructures by droplet evaporation, *Nanoscale* 10 (1) (2018) 142–149. [doi:10.1039/c7nr05767a](#).
- [222] J. T. Wen, C.-M. Ho, P. B. Lillehoj, Coffee ring aptasensor for rapid protein detection, *Langmuir* 29 (26) (2013) 8440–8446. [doi:10.1021/la400224a](#).
- [223] I. Mansoor, B. Stoeber, PIV measurements of flow in drying polymer solutions during solvent casting, *Experiments in Fluids* 50 (5) (2011) 1409–1420. [doi:10.1007/s00348-010-1000-3](#).
- [224] I. Mansoor, U. O. Hafeli, B. Stoeber, Hollow out-of-plane polymer microneedles made by solvent casting for transdermal drug delivery, *Journal of Microelectromechanical Systems* 21 (1) (2012) 44–52. [doi:10.1109/JMEMS.2011.2174429](#).
- [225] F. Zhou, Y. Liu, H. Wang, Y. Wei, G. Zhang, H. Ye, M. Chen, D. Ling, Au-nanorod-clusters patterned optical fiber SERS probes fabricated by laser-induced evaporation self-assembly method, *Optics Express* 28 (5) (2020) 6648. [doi:10.1364/oe.386215](#).
- [226] T. L. Bergman, A. S. Lavine, F. P. Incropera, D. P. DeWitt, *Fundamentals of Heat and Mass Transfer*, 7th Edition, John Wiley & Sons, 2011.
- [227] T. Okuzono, K. Ozawa, M. Doi, Simple model of skin formation caused by solvent evaporation in polymer solutions, *Physical Review Letters* 97 (13). [doi:10.1103/physrevlett.97.136103](#).
- [228] C. W. J. Berendsen, J. C. H. Zeegers, G. C. F. L. Kruis, M. Riepen, A. A. Darhuber, Rupture of thin liquid films induced by impinging air-jets, *Langmuir* 28 (26) (2012) 9977–9985. [doi:10.1021/la301353f](#).
- [229] Y. O. Popov, Evaporative deposition patterns: Spatial dimensions of the deposit, *Physical Review E* 71 (3). [doi:10.1103/physreve.71.036313](#).
- [230] R. Zheng, Y. O. Popov, T. A. Witten, Deposit growth in the wetting of an angular region with uniform evaporation, *Physical Review E* 72 (4). [doi:10.1103/physreve.72.046303](#).
- [231] K. S. Kolegov, L. Y. Barash, Joint effect of advection, diffusion, and capillary attraction on the spatial structure of particle depositions from evaporating droplets, *Physical Review E* 100 (3). [doi:10.1103/physreve.100.033304](#).
- [232] R. Bhardwaj, X. Fang, D. Attinger, Pattern formation during the evaporation of a colloidal nanoliter drop: a numerical and experimental study, *New Journal of Physics* 11 (7) (2009) 075020. [doi:10.1088/1367-2630/11/7/075020](#).
- [233] R. Bhardwaj, X. Fang, P. Somasundaran, D. Attinger, Self-assembly of colloidal particles from evaporating droplets: Role of DLVO interactions and proposition of a phase diagram, *Langmuir* 26 (11) (2010) 7833–7842. [doi:10.1021/la9047227](#).
- [234] F. Doumenc, B. Guerrier, Drying of a solution in a meniscus: A model coupling the liquid and the gas phases, *Langmuir* 26 (17) (2010) 13959–13967. [doi:10.1021/la1018373](#).
- [235] F. Doumenc, B. Guerrier, Self-patterning induced by a solutal marangoni effect in a receding drying meniscus, *EPL (Europhysics Letters)* 103 (1) (2013) 14001. [doi:10.1209/0295-5075/103/14001](#).
- [236] L. Frastia, A. J. Archer, U. Thiele, Dynamical model for the formation of patterned deposits at receding contact lines, *Physical Review Letters* 106 (7) (2011) 077801. [doi:10.1103/physrevlett.106.077801](#).
- [237] L. Frastia, A. J. Archer, U. Thiele, Modelling the formation of structured deposits at receding contact lines of evaporating solutions and suspensions, *Soft Matter* 8 (44) (2012) 11363. [doi:10.1039/c2sm26574e](#).
- [238] T. Okuzono, M. Kobayashi, M. Doi, Final shape of a drying thin film, *Physical Review E* 80 (2). [doi:10.1103/physreve.80.021603](#).
- [239] T. Okuzono, M. Doi, Effects of elasticity on drying processes of polymer solutions, *Physical Review E* 77 (3). [doi:10.1103/physreve.77.030501](#).
- [240] P. V. Lebedev-Stepanov, R. M. Kadushnikov, S. P. Molchanov, A. A. Ivanov, V. P. Mitrokhin, K. O. Vlasov, N. I. Rubin, G. A. Yurasik, V. G. Nazarov, M. V. Alifimov, Self-assembly of nanoparticles in the microvolume of colloidal solution: Physics, modeling, and experiment, *Nanotechnologies in Russia* 8 (3) (2013) 137–162. [doi:10.1134/S1995078013020110](#).
- [241] P. Lebedev-Stepanov, K. Vlasov, Simulation of self-assembly in an evaporating droplet of colloidal solution by dissipative particle dynamics, *Colloids and Surfaces A: Physicochemical and Engineering Aspects* 432 (2013) 132–138. [doi:10.1016/j.colsurfa.2013.05.012](#).
- [242] T. Andac, P. Weigmann, S. K. P. Velu, E. Pinçe, G. Volpe, G. Volpe, A. Callegari, Active matter alters the growth dynamics of coffee rings, *Soft Matter* 15 (7) (2019) 1488–1496. [doi:10.1039/c8sm01350k](#).
- [243] A. Oron, S. H. Davis, S. G. Bankoff, Long-scale evolution of thin liquid films, *Reviews of Modern Physics* 69 (3) (1997) 931–980. [doi:10.1103/revmodphys.69.931](#).
- [244] B. J. Fischer, Particle convection in an evaporating colloidal droplet, *Langmuir* 18 (1) (2002) 60–67. [doi:10.1021/la015518a](#).
- [245] H. Hu, R. G. Larson, Analysis of the microfluid flow in an evaporating sessile droplet, *Langmuir* 21 (9) (2005) 3963–3971. [doi:10.1021/la047528s](#).
- [246] L. Barash, Marangoni convection in an evaporating droplet: Analytical and numerical descriptions, *International Journal of Heat and Mass Transfer* 102 (2016) 445–454. [doi:10.1016/j.ijheatmasstransfer.2016.06.042](#).
- [247] S. J. Kang, V. Vandadi, J. D. Felske, H. Masoud, Alternative mechanism for coffee-ring deposition based on active role of free surface, *Physical Review E* 94 (6). [doi:10.1103/physreve.94.063104](#).
- [248] B. M. Weon, J. H. Je, Self-pinning by colloids confined at a contact line, *Phys. Rev. Lett.* 110 (2013) 028303. [doi:10.1103/PhysRevLett.110.028303](#).
- [249] T. Okuzono, N. Aoki, T. Kajiya, M. Doi, Effects of gelation on the evaporation rate of polymer solutions, *Journal of the Physical Society of Japan* 79 (9) (2010) 094801. [doi:10.1143/jpsj.79.094801](#).
- [250] Y. Y. Tarasevich, I. V. Vodolazskaya, O. P. Isakova, Desiccating colloidal sessile drop: dynamics of shape and concentration, *Colloid and Polymer Science* 289 (9) (2011) 1015–1023. [doi:10.1007/s00396-011-2418-8](#).
- [251] J. Y. Kim, B. M. Weon, Evaporation of strong coffee drops, *Applied Physics Letters* 113 (18) (2018) 183704. [doi:10.1063/1.5049606](#).
- [252] M. Dietzel, D. Poulikakos, Laser-induced motion in nanoparticle suspension droplets on a surface, *Physics of Fluids* 17 (10) (2005) 102106. [doi:10.1063/1.2098587](#).
- [253] M. Yamamura, T. Uchinomiya, Y. Mawatari, H. Kage, Drying-induced

- surface roughening of polymeric coating under periodic air blowing, *AIChE Journal* 55 (7) (2009) 1648–1658. doi:10.1002/aic.11783.
- [254] T. A. Arshad, R. T. Bonnecaze, Templated evaporative lithography for high throughput fabrication of nanopatterned films, *Nanoscale* 5 (2) (2013) 624–633. doi:10.1039/c2nr31924a.
- [255] K. S. Kolegov, Simulation of patterned glass film formation in the evaporating colloidal liquid under IR heating, *Microgravity Science and Technology* 30 (1-2) (2018) 113–120. doi:10.1007/s12217-017-9587-0.
- [256] K. S. Kolegov, Formation of ring structures in a drying under the mask film of colloidal solution, *Bulletin of the South Ural State University. Series "Mathematical Modelling, Programming and Computer Software"* 7 (1) (2014) 24–33, in Russian. doi:10.14529/mmp140103.
- [257] K. S. Kolegov, A. I. Lobanov, Numerical study of mass transfer in drop and film systems using a regularized finite difference scheme in evaporative lithography, *J. Samara State Tech. Univ., Ser. Phys. Math. Sci.* 22 (2) (2018) 344–363, in Russian. doi:10.14498/vsgtu1601.
- [258] Y. Y. Tarasevich, I. V. Vodolazskaya, L. V. Sakharova, Mathematical modeling of pattern formation caused by drying of colloidal film under a mask, *The European Physical Journal E* 39 (2) (2016) 26. doi:10.1140/epje/i2016-16026-5.
- [259] I. V. Vodolazskaya, Y. Y. Tarasevich, Modeling of mass transfer in a film of solution evaporating under the mask with holes, *The European Physical Journal E* 40 (10). doi:10.1140/epje/i2017-11574-8.
- [260] S. Hu, Y. Wang, X. Man, M. Doi, Deposition patterns of two neighboring droplets: Onsager variational principle studies, *Langmuir* 33 (23) (2017) 5965–5972. doi:10.1021/acs.langmuir.7b01354.
- [261] K. Efimenko, J. Finlay, M. E. Callow, J. A. Callow, J. Genzer, Development and testing of hierarchically wrinkled coatings for marine antifouling, *ACS Applied Materials & Interfaces* 1 (5) (2009) 1031–1040. doi:10.1021/am9000562.